Characterisation of $CaCO_3$ phases during strain-specific ureolytic precipitation

Alexandra Clarà Saracho[1,*], Stuart K. Haigh[1], Toshiro Hata[2], Kenichi Soga[3], Stefan Farsang[4], Simon A. T. Redfern[5], and Ewa Marek[1]

[1]University of Cambridge, Department of Engineering, Cambridge, CB2 1PZ, UK
[2]Hiroshima University, Department of Engineering, Hiroshima, 739-8527, Japan
[3]University of California-Berkeley, Department of Engineering, CA 94720, California, USA
[4]University of Cambridge, Department of Earth Sciences, CB2 3EQ, Cambridge, UK
[5]Asian School of the Environment, 50 Nanyang Avenue, Nanyang Technological University, Singapore 639798
[*]ac989@cam.ac.uk

ABSTRACT

Numerous microbial species can selectively precipitate mineral carbonates with enhanced mechanical properties, however, understanding exactly how they achieve this control represents a major challenge in the field of biomineralisation. We have studied microbial induced calcium carbonate ($CaCO_3$) precipitation (MICP) in three ureolytic bacterial strains from the *Sporosarcina* family, including *S. newyorkensis*, a newly isolated microbe from the deep sea. We find that the interplay between structural water and strain-specific amino acid groups is fundamental to the stabilisation of vaterite and that, under the same conditions, different isolates yield distinctly different polymorphs. The latter is found to be associated with different urease activities and, consequently, precipitation kinetics, which change depending on pressure-temperature conditions. Further, $CaCO_3$ polymorph selection also depends on the coupled effect of chemical treatment and initial bacterial concentrations. Our findings provide new insights into strain-specific $CaCO_3$ polymorphic selection and stabilisation, and open up promising avenues for designing bio-reinforced geo-materials that capitalise on the different particle bond mechanical properties offered by different polymorphs.

Calcium carbonate ($CaCO_3$) makes up almost 4% of the Earth's crust and has been studied extensively due to its importance in biomineralisation in natural environments, including carbon cycling, alkalinity generation, and the biogeochemical cycling of elements[1–3]. In addition to its importance in nature, however, the enhanced mechanical properties of certain biotic calcium carbonates have inspired many studies to try to understand their structural "secrets"[4–6], and prompted their use in geotechnical engineering to improve the mechanical response of soils[7–11]. A clear example of these natural materials is nacre in mollusc shells, formed of microlaminate composites of aragonite and/or calcite, each with an associated organic matrix that gives them a fracture toughness 3000 times greater than that of the constituent mineral alone[12]. Clearly, the coupling of a mineral phase with an organic material (*i.e.* biomineral) plays a vital role in the formation and stabilisation of the final $CaCO_3$ precipitate, in addition to contributing to its ultimate mechanical properties[4,13–17]. However, understanding the interrelationship between biotic precipitation, polymorphism, and long-term stabilisation has proven to be far from trivial.

It is well established that $CaCO_3$ has three polymorphs: vaterite, aragonite, and calcite, with rhombohedral, orthorhombic and hexagonal structures respectively, in order of decreasing solubility and increasing thermodynamic stability[18]. Additional metastable forms have been noted in the literature, all of which are hydrated: monohydrocalcite ($CaCO_3 \cdot H_2O$), ikaite ($CaCO_3 \cdot 6\,H_2O$), calcium carbonate hemihydrate ($CaCO_3 \cdot \frac{1}{2}\,H_2O$), and amorphous calcium carbonate (ACC)[19,20]. Thus far, most studies have tackled the formation and crystallisation of $CaCO_3$ in abiotic systems, with a particular focus on ACC and vaterite as intermediates in the crystallisation of $CaCO_3$[21–25]. However, in contrast to the unique nature of the equilibrium state, multiple reaction pathways from a given initial condition to that final state of thermodynamic equilibrium may exist. Such reaction pathways can be very sensitive to minor impurities and environmental perturbations, such as the presence of microorganisms, which modify the energy barrier from reactant to product phases[26]. It has even been suggested that organic macromolecules associated with bacterial activity cause the Ostwald step sequence to stop at one of its intermediate stages: ACC $\rightarrow$ vaterite $\rightarrow$ calcite[21], making biotic vaterite precipitation far more common than would be anticipated in abiotic systems. From a chemical standpoint, the polymorphous composition is governed by the addition of the reactants, which lead to a supersaturation state in which the concentration of calcium and carbonate ions exceed the solubility product of $CaCO_3$[18,27]. This simultaneously triggers the nucleation of crystals and the dissolution of the colloidal ACC precursor[18]. However, local variations of the calcium and carbonate ion activity product (IAP) and thus saturation, can favour the formation

of one polymorph over another. Vaterite, for example, typically precipitates in highly supersaturated and moderately alkaline environments[14,21,23].

Within this context, enzymatic hydrolysis of urea presents a straightforward process to understand the precise role of microbes in microbial induced calcium carbonate precipitation (MICP). This is because the urease enzyme is ubiquitous in microorganisms, yeast, and plants[5,28]. In addition, it can be easily induced using inexpensive chemicals and is the most widely used process in biomediated soil improvement applications. Ureolytic bacteria enzymatically hydrolyse urea ($CO(NH_2)_2$), resulting in the production of ammonium (NH_4^+) and dissolved inorganic carbon (DIC), which in turn increase pH and favour $CaCO_3$ precipitation in the presence of soluble calcium ions (Equation 1). This study focuses on three different ureolytic bacterial strains, all belonging to the *Sporosarcina* species: *Sporosarcina pasteurii* (ATCC 11859), *Sporosarcina aquimarina* (ATCC BAA-723), and *Sporosarcina newyorkensis*–a newly isolated microbe from the deep sea in offshore Japan extracted by the National Institute of Advanced Industrial Science and Technology (AIST) using pressure-core nondestructive analysis tools[29]. To our knowledge, this has never been studied before. These strains were selected as they proliferate in different isolation environments: surface dry conditions, and shallow and deep sea, respectively.

$$CO(NH_2)_2 + 2\,H_2O \longrightarrow 2\,NH_4^+ + CO_3^{2-} \tag{1a}$$

$$CO_3^{2-} + Ca^{2+} \longrightarrow CaCO_3\downarrow \tag{1b}$$

Our aim is to shed light on the interaction between the components of mineralised biological materials involved in $CaCO_3$ precipitation–namely minerals, macromolecules and water–, and understand their influence on the stabilisation of different $CaCO_3$ polymorphs. In addition, we wish to understand how strain-specific precipitation kinetics promote and affect this process. For this purpose, $CaCO_3$ was precipitated *in vitro* in 14 mL test tubes via the three different ureolytic soil bacteria described above. To ensure analogous reference conditions, strains were cultivated under sterile conditions at the same pressure and temperature–*i.e.* $P = P_{atm}$ and $T = 30\,^{\circ}C$–to an optical density (OD_{600}) of ~ 0.5, and subsequently subject to identical external treatment conditions. The cementation treatment liquid medium consisted of a premixed solution of an equimolar amount of urea and $CaCl_2$ (0.3 M), in addition to $3\,g\,L^{-1}$ of Nutrient Broth, all dissolved in deionised water. All samples were created using a ratio of bacteria solution to cementation solution of 1:2. Results strongly suggest that the presence of structural water together with specific amino acids is fundamental to the stabilisation of vaterite and that, at the same initial OD_{600} and treatment conditions, different strains yield distinctly different polymorphs. For this reason, we compared the precipitation kinetics, and the pressure-temperature dependence of bacterial population and urease activity for the three microorganisms. Finally, *S. pasteurii*–which is the most common soil bacterium used in geotechnical engineering applications–was also investigated under varying urea-$CaCl_2$ solution concentrations and initial OD_{600}. The mineralogy, morphology, and properties of precipitates were characterised using an array of complementary techniques, namely thermogravimetric analysis coupled with mass spectroscopy (TGA-MS), Raman spectroscopy (RM), X-ray powder diffraction (XRD), and scanning electron microscopy (SEM); and the precipitation kinetics of the three microorganisms quantified through measurement of calcium ion (Ca^{2+}) concentrations and pH (Table S4). Ultimately, our results suggest that strain-specific $CaCO_3$ precipitation occurs during ureolytic MICP, possibly due to differences in the urease enzyme, and its response to treatment concentrations and pressure-temperature variations, and that $CaCO_3$ polymorphism in biotic systems is far more common than previously anticipated. This may have significant implications for biomediated soil improvement systems.

Results

Amorphous and crystalline $CaCO_3$ polymorphs

XRD analysis (Figure 1a) revealed that calcite was the primary polymorph that precipitated in the presence of *S. newyorkensis* (SN01-0.3 M), along with small traces of halite resulting from the drying of the marine broth media used to cultivate the isolate[30] (Figure S1). On the other hand, precipitates of *S. aquimarina* (SA01-0.3 M) contained vaterite as a secondary phase to calcite. The XRD spectrum of precipitates of *S. pasteurii* (SP01-0.3 M) showed no traces of calcite, but a broad hump in the range of 15-40° 2Θ consistent with the presence of a poorly-ordered material and matching data reported in the literature for ACC[31,32].

Thermal analysis of the same samples also showed significant differences (Figure 1b). *S. newyorkensis* was characterised by the occurrence of three main weight loss steps, at 217 °C, 438 °C, and 757 °C, corresponding to 2.4, 9.1, and 38.1 wt%, respectively. In contrast, the TGA of precipitates of *S. aquimarina* only showed two main weight loss steps at approximately 300 °C and 717 °C. However, the first derivative (DTG) revealed that the former resulted from the overlap of four peaks at 184 °C, 251 °C, 287 °C, and 348 °C (Figure S2). These values appeared too high to be attributed to physisorbed water–*i.e.* water evaporated below 115 °C[19]–and were thus attributed to weakly ($\sim 30-200\,^{\circ}C$) and strongly ($\sim 200-550\,^{\circ}C$) bound water molecules, giving a structural water content of 8.0 wt% from TGA[33]. Furthermore, the large weight loss observed for *S. newyorkensis* and *S. aquimarina* at 757 °C and 717 °C (36.4 wt%), respectively, was consistent with the loss of CO_2 from

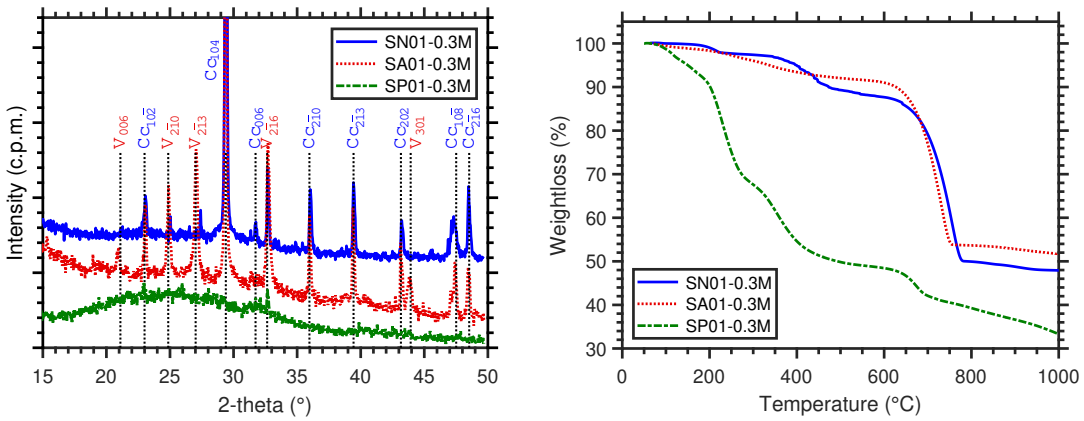

Figure 1. XRD pattern with *hkl* values of Bragg peaks indicated (Cu-Kα radiation, $\lambda = 1.5406$ Å) (a); and TG curves (All: heating rate 10 °C min^{-1}; SN01-0.3 M: Ar "reactive gas" flow rate 50 mL min^{-1}, and SA01-0.3 M and SP01-0.3 M: N_2 "reactive gas" flow rate 50 mL min^{-1} (b) of precipitated $CaCO_3$. V, vaterite; Cc, calcite; Halite peaks resulting from desiccating media of *S. newyorkensis* not indicated.

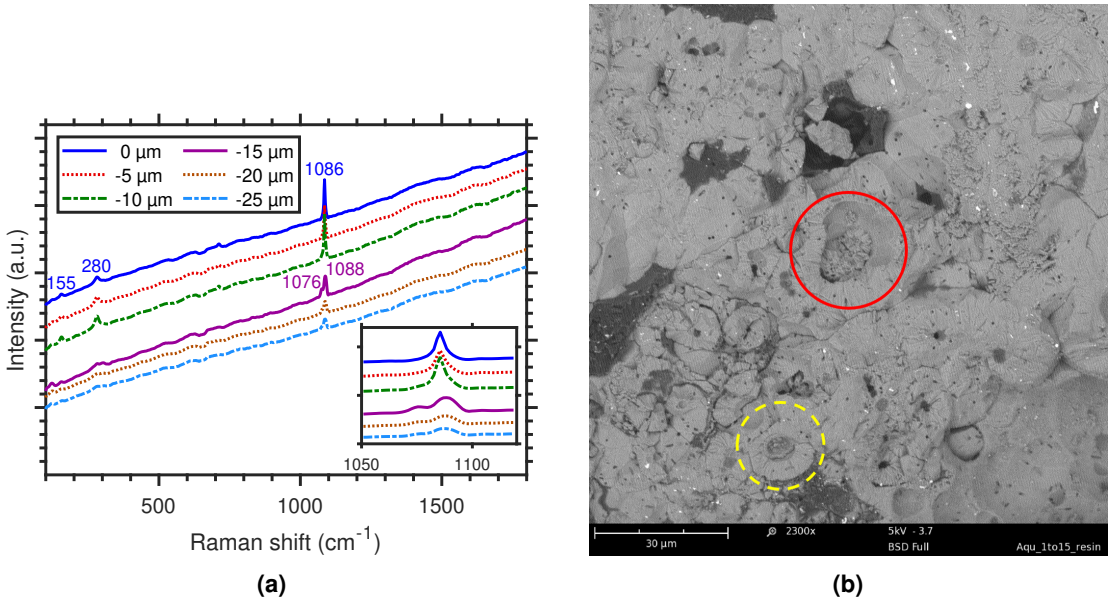

Figure 2. Raman spectra of polymorphic $CaCO_3$ crystals formed in the presence of *S. aquimarina* (SA01-0.3 M) evidencing the coexistence of calcite and vaterite within a "single crystal" and showing their spatial arrangement (a); and SEM BSE image of internal structure of biotic precipitates of *S. aquimarina* with some cores showing traces of vaterite spherulites (yellow dotted circle) and others that have started to be filled by advancing crystallisation steps (red solid circle) (b).

the carbonate decomposition, and also provided an independent confirmation that both samples were comprised almost solely of $CaCO_3$ phases. Regarding the precipitates of *S. pasteurii*, TGA revealed that below 250 °C there were two distinguishable temperature intervals where weight losses occurred, namely at 112 °C and 231 °C. The total weight loss in these transitions was 27 wt% (after physisorbed water removal) and was attributed to dehydration and crystallisation of ACC[34]. The third weight loss was 18 wt% and occurred in the temperature range of 300-550 °C. At such high temperatures, this was unlikely to be caused by the release of structural water, and was thus associated with the pyrolysis of macromolecules, either of organic or inorganic origin. Finally, the thermal peak at 670 °C, matching the decarboxylation of $CaCO_3$, only accounted for 8 wt% of the weight loss, indicating that minor amounts of $CaCO_3$ were present. The final plateau, slightly inclined, indicated that final weight constancy was not achieved in this sample, possibly due to kinetic effects upon carbonate decomposition[33].

Biotic vaterite precipitation

To further investigate how vaterite and calcite were spatially organised, the precipitates of *S. aquimarina* were examined through Raman spectroscopy. Firstly, spectra were acquired at two visually distinct points of a "single crystal". Results are shown in Figure S3, together with an optical microscopy image of the target collection points. The most prominent features of calcite are the symmetric stretching mode (ν_1) of the carbonate group, followed by two external modes[35,36]. These appeared at 1085 cm^{-1} with a full width at half maximum (FWHM) of 7 cm^{-1}, and at 155 and 280 cm^{-1}, respectively. The identification of other features was not possible due to the high background noise. Raman spectroscopy also helped distinguish vaterite from calcite by comparing the wave numbers of the ν_1 mode. Indeed, the absorption bands at 1076 and 1088 cm^{-1} corresponding to the symmetric stretching of vaterite[37] were detected in one of the spectra shown in Figure S3. Secondly, spectra of a "single crystal" were also collected up to a penetration depth of 25 µm, with results clearly showing a polymorph transition (Figure 2a). While the characteristic single peak of calcite at 1086 cm^{-1} was detected at the surface, the two peaks at 1076 cm^{-1} and 1088 cm^{-1} appeared within the internal structure. Moreover, the broad nature of the vaterite peak at 1088 cm^{-1} could possibly suggest the combination of two peaks at 1090 and 1085 cm^{-1}, the latter being associated to calcite. This is due to the peak convolution between the polymorphs in this region. In addition, the disappearance of the two lower frequency lattice modes (155 and 280 cm^{-1}) with penetration depth further supported a transition between carbonate phases. Table S1 lists the peak positions and the corresponding assignments of calcite and vaterite to illustrate the comparison between precipitates of *S. newyorkensis* and *S. aquimarina*.

SEM images of precipitates of *S. aquimarina* showed two distinctive morphologies: (a) spherulites, 5-50 µm in diameter (Figure S4a) , which were associated to vaterite and (b) disphenoid- and dipyramid-like calcite crystals (Figure S4e). Numerous rod-shaped bacterial cells (with length $\sim$ 2 µm and a diameter of $\sim$ 0.5 µm) were observed encased within the growing spherulites, suggesting that the presence of *S. aquimarina* was a prerequisite for their formation. This was further reinforced by the presence of smooth dumbbell $CaCO_3$ morphologies, which have been reported to be uniquely bacterial in origin (Figure S4b)[38]. In addition, an epoxy cast cross-section of the precipitates (Figure 2b) revealed hollow cores with walls formed by a fibro-radial internal structure, an observation consistent with spherulite surface features described by[39]. While some cores still showed traces of vaterite spherulites, others had started to be filled by advancing crystallisation steps. Further key aspects of the incorporation of the vaterite spherulites into the calcite crystals were obtained by comparing Figure S4b-e.

Indirect evidence for structural amino acids and water

As evidenced by Figure S8a-b, the XRD and Raman spectroscopy of precipitates of *S. aquimarina* and *S. newyorkensis* also showed the presence of additional absorption bands that did not correspond to carbonate phases. In particular, the Raman spectra showed the Disorder (D) and Graphite (G) bands typical for organic carbons, with those present in precipitates of *S. newyorkensis* (SN01-0.3 M) exhibiting a slightly lower level of organisation than those observed within preciptates of *S. aquimarina* (SA01-0.3 M) (see zoomed in plot Figure S8b and associated supplementary discussion, and Table S2). Consequently, TG-MS analysis on two different powdered samples was used to identify and monitor the evolution of the exhaust gases. MS was set to detect certain m/z values associated with common fragments from molecular-ions, listed in Table S3. All

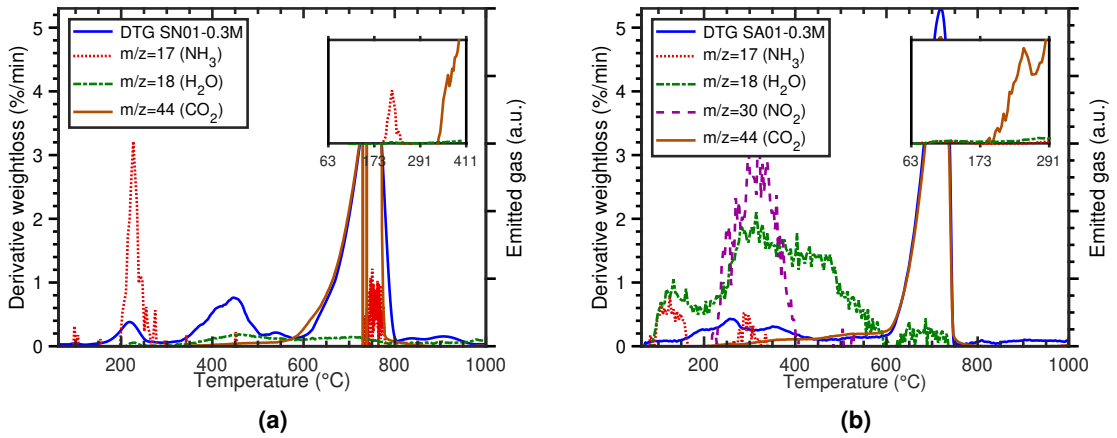

Figure 3. DTG and mass spectra of evolved gases measured from coupled TG-MS of $CaCO_3$ crystals formed in the presence of: (a) *S. newyorkensis* (heating rate 10 °C min^{-1}; Ar "reactive gas" flow rate 50 mL min^{-1}); and (b) *S. aquimarina* (heating rate 10 °C min^{-1}; N_2 "reactive gas" flow rate 50 mL min^{-1}).

MS signals were normalised to a baseline shift value obtained after each experiment from a blank run using an empty crucible. Results therefore refer to relative incremental yields rather than absolute intensity values *per se*. The advantage of this was to be able to compare all exhaust gases using a single plot, allowing for thermal decomposition sequences to be unequivocally identified. The only exception was CO_2, plotted on its own intensity axis because its relative yield was considerably higher than that of the other products–understandable given that all of the analysed precipitates were carbonates. Therefore, where discussion warranted, zoomed in plots of the range of temperatures of interest showing the CO_2 yield with respect to the other products in the group were presented.

The TGA of precipitates of *S. newyorkensis* showed the occurrence of three main weight loss steps. As shown in Figure 3a, CO_2 was the main gaseous product in the third step (757 °C), associated with the decarbonation of $CaCO_3$. Regarding the first and second steps (217 and 438 °C), decomposition products mainly included NH_3 and H_2O, respectively. This indirectly demonstrated the presence of amino acids within the precipitated carbonates and suggested that their primary decomposition included deamination with low yields of dehydration. Using Fourier transform infrared spectroscopy (FTIR), previous studies identified the presence of amino acids within the $CaCO_3$ structure of biotic precipitates by the amide I signature at 1655 cm^{-1}[14,40,41]. Further, FTIR for evolved gas analysis coupled to TGA revealed that the thermal decomposition of organics results in the release of CO, CO_2 and NO_2 in the temperature range of $150-500$ °C, while amino acids in biotic carbonates also involve the release of NH_3[14]. These results are in agreement with the TG-MS analyses reported here. Moreover, Figure 3a shows that the rapid releasing rate of NH_3 in the first stage was in sharp contrast with the longer H_2O and NH_3 releases observed in both the second and third stages respectively, revealing different pathways of formation. In the former, NH_3 was most likely lost as a result of a primary decomposition (*i.e.* individual molecular decomposition of amino acids or formation of an amino radical), while H_2O in the second stage may have been produced following secondary reactions[42,43]. One interesting observation was that CO_2 was not released during the first stage (see zoomed in plot of Figure 3a), suggesting that less common aromatic β-amino acids were present[42] (Figure S8b).

Regarding precipitates of *S. aquimarina*, their pyrolysis was markedly different (Figure 3b), with the first two decompositions being less sharp and partially overlapping. The most conspicuous feature was that water remained a structural constituent up to 600 °C, gradually being released from 100 °C (8 wt%). Additionally, the fragmentation products and sequence of precipitates indirectly suggested different starting amino acids, with deamination being a primary, although minor, mode of decomposition. This was echoed by the small NH_3 peak measured between 100-160 °C, previously observed during the pyrolysis of α-amino acids and attributed to the existence of an intermediate[44]. On the other hand, a second process, also considered to be a primary decomposition mode, was the decarboxylation reaction of α-amino acids to produce CO_2 and amines[42,44]. This was evidenced by the CO_2 peak measured at 243 °C (see zoomed in plot of Figure 3b). Following this primary decomposition, a number of secondary products arise, possibly from the fragmentation of the amines themselves (see supplementary discussion for further details on the pyrolysis of amino acids).

$CaCO_3$ precipitation kinetics

With approximately equal $OD_{600} \sim 0.5$ but different (specific) urease activities (Table S4), it is suggested that the mineralogy, morphology and properties of the precipitated $CaCO_3$ can be controlled by ureolytic strains with different urease activities and, consequently, precipitation kinetics–quantified through measurement of calcium ion (Ca^{2+}) concentrations and pH[45].

Equal concentrations of Ca^{2+} ions and bacterial densities were initially present in all tests, with CO_3^{2-} ion concentrations being equal to zero until the onset of urea hydrolysis. As a result, initial calcium depletion rate–calculated as the change in Ca^{2+} ion concentration over a certain period of time, dCa^{2+}/dt–was most closely associated with the nucleation of $CaCO_3$ for each microorganism[45]. A lower initial urease activity was associated with a faster initial calcium depletion rate from solution (*cf.* Table S4 and Figure 4a). Comparing the results for *S. pasteurii* (SP01-0.3 M) with those for *S. newyorkensis* (SN01-0.3 M) and *S. aquimarina* (SA01-0.3 M) it is clear that *S. pasteurii*'s metabolic activity was able to initially hydrolyse more urea into CO_3^{2-} ions in the same period of time. This resulted in alkalinity generation and ammonia release, which respectively caused a rapid increase in supersaturation and pH. This provided the high crystallisation kinetics needed for the spherulitic precipitation of ACC, which proceeds via a fast nucleation-controlled mechanism[46]–again evidenced by the higher initial calcium depletion rate. Further, the ACC-vaterite transformation in precipitates of *S. aquimarina* manifested by a slow decrease in pH associated with the release of water molecules during dissolution; and by a decreasing Ca^{2+} depletion rate associated with the release of Ca^{2+} ions stored in ACC and their re-precipitation into vaterite. Conversely, this dissolution (and associated pH drop) was not observed in SP01-0.3 M, further reinforcing the stabilisation of ACC.

The initial Ca^{2+} depletion rate was smallest for *S. newyorkensis*, indicating a slower nucleation event. Interestingly, this reversed as Ca^{2+} ions returned to solution, suggesting the early dissolution of Ca-containing precipitates (most likely ACC). As with the initial calcium depletion rate, the timing of this transition appeared to depend on the microorganism. For *S. newyorkensis*, with the highest urease activity, this transition occurred earlier than for the other two less ureolytic microorganisms. Figure 4b further suggests that this process was highly pH-dependant. For *S. newyorkensis* (pH $\approx 7-7.5$),

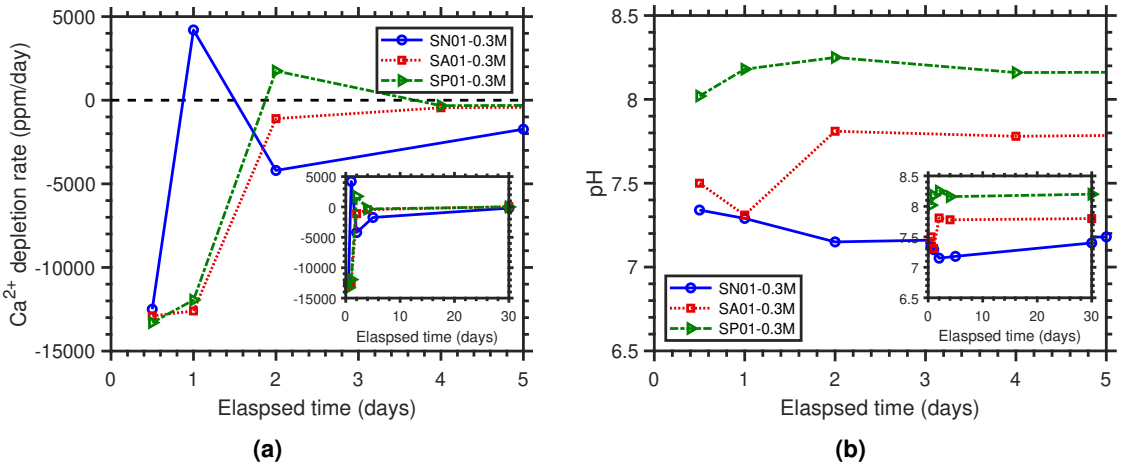

Figure 4. Time evolution of the (a) rate of calcium depletion and (b) pH.

calcium ions returned to solution within the first 24 h, and depleted again following a second nucleation event (calcite). This reinforced a direct ACC-calcite transformation when initial pH values are closer to neutral suggested in the literature[46]. With increased pH however, vaterite (pH $\approx 7.5-7.8$) and ACC (pH $\approx 7.8-8.3$) were stabilised by *S. aquimarina* and *S. pasteurii*, respectively. This was linked to a delayed return of Ca^{2+} to solution.

An additional consideration is that the pressure-temperature conditions in the environments where the three bacterial strains proliferate are substantially different, thus affecting bacterial growth and urease activity. These parameters were therefore investigated during a 4-day cultivation at two different pressures (1 atm, 3 MPa) and three different temperatures (4 °C,15 °C,30 °C). Interestingly, results showed that the effect of temperature on OD_{600} was more pronounced than that of pressure (Figures S5a and S6a), and that (specific) urease activity was most sensitive to pressure at temperatures near those of the original isolation environment (Figure S5b,c). Figure S6b shows that a loss of specific urease activity with pressure for all three ureolytic microorganisms, suggesting that pressure potentiates inhibitory factors that affect the function of the urease enzyme. It is also clear that aside from pressure and temperature, time played an important role, with the following conditions yielding a maximum specific urease activity (all at $P = 1$ atm): *S. newyorkensis*, 1-day cultivation, $T = 4$ °C; *S. aquimarina*, 1-day cultivation, $T = 15$ °C; and *S. pasteurii:* 4-day cultivation, $T = 30$ °C.

Cooperative effect of bacterial and treatment concentrations

We further extended our study by investigating the influence of OD_{600} and urea-$CaCl_2$ solution molarity on polymorphic selection for *S. pasteurii* (Figure S7). For example, SP00-0.02 M-D refers to *S. pasteurii* treated with 0.02 Molar of $CaCl_2$ and with a diluted OD_{600} of 1.38. TGA showed that samples treated with 0.02 and 0.2 M displayed almost identical thermogram profiles between bacterial concentrations (Figure S7a-d). Close examination of the 0.02 M samples (D and ND) disclosed that in both cases the amount of $CaCO_3$ was $\sim$ 15-30 wt%, which was found to be in agreement with values reported in other biotic studies of ACC[15,47]. Furthermore, two distinguishable temperature intervals where weight loss occurred were measured below 250 °C. These were accompanied by broad peaks at around 110 and 230 °C and were attributed to the release of water molecules. This double dehydration behaviour was also consistent with previous studies[15,47,48]. The total weight loss in this transition was 15-16 wt%, which was compatible with a stoichiometry of $CaCO_3 \cdot H_2O$. Finally, a third weight loss region of approximately 25 wt% occurred in the temperature range of 250-500 °C. At such high temperatures, this loss could be attributed to either strongly bound water molecules and/or to the secondary decomposition of amines (*cf.* Figure 3a). The wider nature of this peak (*i.e.* slower release), however, lent some support to the existence of secondary reactions (see supplementary discussion on the pyrolysis of ACC and Figure S12). Acquisition of XRD patterns for the 0.02 M samples was not possible due to the low volume of precipitates available. However, the similarities between the thermal decomposition observations made for these samples and SP01-0.3 M, allowed us to conclude that XRD patterns would have been very similar to the one showed in Figure 1a and attributed to ACC.

The TGA of precipitates resulting from the 0.2 M solutions (both D and ND) showed a clear peak at around 760 °C ($\sim$40 wt%), corresponding to the decomposition of $CaCO_3$. In addition, their TG profiles were very similar to the profile obtained for precipitates of *S. aquimarina* (*c.f.* Figure 1b), with two small peaks at approximately 220 °C and 320 °C (8.2 wt%). Taken together, these results corroborated the presence of water within the crystal structure with a stoichiometry of $CaCO_3 \cdot \frac{1}{2} H_2O$[19]. In addition, the XRD measurements showed the presence of both vaterite and calcite, but no extra reflections attributed to

crystalline hydrated phases were apparent (Figure S7e,f).

Bacterial concentration had a greater effect at a solution concentration of 1 M, with calcite being the only phase detected at high OD_{600} (SP03-1 M-ND Figure S7f) and vaterite at low OD_{600} (SP02-1 M-D Figure S7e). The TGA of these samples provided further valuable insights into their properties. While SP03-1 M-ND (Figure S7b,d) showed a sharp peak at 240 °C–matching the first peak observed for *S. newyorkensis* (*cf.* Figure 3a) and associated to the pyrolysis of amino acids–, the thermal decomposition of SP01-1 M-D (Figure S7a,c) started at a lower temperature (220 °C) and was accompanied by a second peak at 327 °C. In consistency with previous observations made for precipitates containing vaterite, and by comparing this profile with the MS results for precipitates of *S. aquimarina* (*cf.* Figure 3b), results strongly suggested the presence of structural water and amino acids. Finally, both samples displayed a significant weight loss at 740 °C, corresponding to the decarbonation of $CaCO_3$.

Discussion

S. aquimarina induced the formation of highly porous rounded polycrystals, which had no well defined structure. Raman spectra collected for a "single crystal" up to a penetration depth of 25 µm showed a transition from calcite to vaterite with depth, evidenced by the splitting of the ν_1 mode into two peaks (Figure 2a). To our knowledge, such Raman characterisation of $CaCO_3$ polymorphs has never before been carried out and provides further evidence that biotic calcite initiates from a metastable phase rather than from a crystalline nucleus leading to single crystals. Moreover, hollow cores with walls formed by a concentric channel-like structure of interconnected pores were observed by SEM and suggested radial growth[49]. While some cores still showed traces of vaterite spherulites, others had already started to be filled by advancing crystallisation steps (Figure 2b). This morphology further reinforced the existence of a metastable precursor, which adopts a spherical structure to minimise its surface contact with the surroundings[15], and provided significant evidence of a vaterite-calcite transformation.

Furthermore, our results indirectly showed that vaterite only stabilised when water molecules and amino acids were present in the crystal structure–*i.e.* SA01-0.3 M and SP01-0.2 M. The idea that organic macromolecules can stabilise vaterite has been suggested previously, both in biotic[14] and abiotic[50,51] systems. However, their presence alone as a justification for stabilisation seems unlikely as precipitates of *S. newyorkensis* only showed calcite peaks despite containing amino acids within their structure (Figures 1a and S1). According to our TGA data, precipitates containing vaterite also comprised of half a molecule of water per one molecule of $CaCO_3$. Therefore, global rationalisation of these results was possible by considering water molecules, potentially from small amounts of additional hydrated phases that become structurally interrelated with the crystal structure. This likely happens via a hydrogen bond between the amino acid surface along the edge of the crystal and the water molecule. This scenario was supported by the different composition of amino acids in precipitates of *S. newyorkensis* and *S. aquimarina* (see supplementary discussion on pyrolysis of amino acids). Hence, our results, as well as those of other studies[52,53], suggest that only specific amino acid groups interact with the $CaCO_3$ surface, thus having an effect on the properties of the precipitated phases. In particular, polar hydrophylic amino acids–*i.e.* those amino acids that have oxygen and nitrogen atoms and with an unequal distribution of electrons–would be the only ones able to form hydrogen bonds with water molecules, either as proton donors or acceptors. The presence of nitrogen during the pyrolysis of precipitates of *S. aquimarina* lent some support to the existence of these hydrophilic amino acids within the crystal structure.

To better understand the underlying mechanisms during strain-specific ureolytic precipitation of $CaCO_3$, the precipitation kinetics were quantified and compared. Results showed that the precipitation (or not) of ACC or vaterite as precursors and/or intermediates of calcite could be favoured by selecting microorganisms with appropriate urease activities, and therefore, precipitation kinetics (*cf.* Figure 4 and Table S4). *S. pasteurii*, the low-urease activity microorganism, had the fastest initial nucleation kinetics, and *S. newyorkensis*, the high-urease activity microorganism, had the slowest initial nucleation kinetics. Subsequently, crystallisation pathways of $CaCO_3$ polymorphs appeared to be highly pH- and dissolution rate-dependant. High pH and longer dissolution times following a fast nucleation event prompted ACC stabilisation (SP01-0.3 M); while a pH closer to neutral and shorter dissolution times following a slower nucleation event promoted an ACC-calcite transformation (SN01-0.3 M). Values for *S. aquimarina* (SA01-0.3 M), yielding an ACC-vaterite-calcite transformation, were in between. Moreover, regardless of the formation pathway, $CaCO_3$ polymorph transformation involved the release of water (and the associated pH drop). Therefore, these results provide additional evidence that controlling dissolution kinetics is essential to controlling polymorph stabilisation. Nonetheless, establishing the specific mechanism via which this occurs requires direct amino acid analysis.

Because the kinetics of mineralisation were found to depend on (specific) urease activity, we sought to understand the role of cultivation conditions. Findings suggest that OD_{600} is most sensitive to temperature, whilst (specific) urease activity displayed a more complex pressure-temperature dependence. The increase in OD_{600} with temperature (Figure S5a), most notable for *S. newyorkensis* and *S. aquimarina*, may, to some extent, be attributed to the decrease in dissolved oxygen contents. Indeed, an oxygen-limited environment would have prompted the growth of (facultative) anaerobic microorganisms. There is however a large body of research supporting the idea that pressure and temperature do not only affect the microbial ecology of aqueous environments, but also the structural stability of biomolecules[54–56], the cell membrane composition[57], and the

physiology of bacterial cells[58]. Therefore, further work is required to assess the role of pressure and temperature on these processes, as well as on how they affect the preferred $CaCO_3$ phase precipitated by the bacterial strains studied here.

Results showed that optimum conditions for $CaCO_3$ polymorphism are both strain- and environment-dependant (*i.e.* urea-$CaCl_2$ solution, pressure, temperature). Under the same bacterial concentrations and environmental conditions the three bacterial strains studied herein produced different polymorphs (Figure 1a), most likely due to the differences in their urea hydrolysis metabolism process. In addition, the results for *S. pasteurii* showed a coupling between the concentration of ions in solution (*i.e.* supersaturation) and the initial bacterial concentrations. Results suggested that the higher the ionic strength, the stronger the interaction between background ions and water becomes. This reduced the availability of water molecules in the solution, favouring clustering and dehydration, and thus precipitation. Conversely, at low ionic strengths, dehydration was hindered due to the higher availability of water molecules in the solution[6]. This promoted hydrophilic interactions between amino acid and water molecules, affecting the dissolution-reprecipitation via which vaterite transforms into calcite. It is worth pointing out that in biotic systems, high ionic strength is attained through the combination of high bacterial concentrations–*i.e.* yielding high carbonate ion concentrations–and high urea-$CaCl_2$ solution concentrations, and it is this trade-off between the two that will determine whether metastable polymorphs stabilise or not.

Implications for geotechnical engineering

As a general rule, calcite has been the only $CaCO_3$ polymorph reported for geotechnical engineering applications, as this is thought to be less prone to alteration, *i.e.* more stable. However, this study supported the notion that ACC and vaterite are much more abundant in $CaCO_3$ biomineralisation than previously believed, and clarifying how they are formed and stabilised may have broader implications for the mechanical properties of cemented sands. Generally speaking, the role of MICP in sands is to create an adhesive bond at the inter-particle contacts, enhancing their load-carrying capacity. In this context, particle contact properties will both be affected by the degree of cementation and the nature of the cementing bond (*e.g.* morphology, mineralogy, properties). Both numerical and experimental data have shown that increasing the cementation level enhances the maximum shear strength and stiffness at small strains, and as the cementation increases the stress-strain behaviour transitions from ductile to brittle[9,59,60]. From an engineering standpoint, this leads to an unwanted soil response because brittle materials absorb little plastic energy prior to fracture, and thus fail catastrophically. Clearly, it is also noted that different $CaCO_3$ polymorphs yield different particle contact properties, leading to variations in their strengthening effect. DEM analyses in the literature have shown that an increase in inter-particle friction brings the stress-strain response of granular materials from ductile to brittle, and augments the anisotropic distribution of contact forces[61]. For the specific case of MICP-treated soils, studies further concluded that increasing calcite content results in a few heavily loaded particle contacts transmitting a large proportion of the load, thus making the force distributions become increasingly non-uniform[59]. This is consistent with the fact that higher friction values tend to decrease the mean contact number per particle[61].

Of key importance therefore, is that the $CaCO_3$ polymorph selection may be controlled through selection of a bacterial strain with appropriate precipitation kinetics, while metastable polymorph stabilisation may be controlled by inhibiting dissolution through the interplay between specific amino acid groups and water within the crystal structure. Further, this study showed that ureolytic microorganisms common to geotechnical engineering environments not only adapt to the urea-$CaCl_2$ solution by modulating the precipitation kinetics, but that this interaction is very sensitive to pressure and temperature. In particular, the increased sensitivity of urease activity to pressure at temperatures near those of the original isolation environment is of major importance for the application of MICP in the deep sea, where both high pressure and low temperature combine to produce a highly hostile environment for bacterial viability.

Results for *S. pasteurii* further revealed that biotic precipitation of calcite alone required both high urea-$CaCl_2$ solution concentrations and high bacterial concentrations, treatment conditions that would yield substantial amounts of ammonium ions (NH_4^+), a hazardous byproduct of urea hydrolysis. However, using a bacterial strain that is able to produce the desired polymorph at lower bacterial and treatment concentrations (*e.g. S. newyorkensis*) offers potential to lower the yield of this byproduct. Therefore, an optimisation exercise between bacterial and treatment concentrations is required on a strain-specific basis for biotechnological applications.

Methods

Bacterial strains and cultivation

Three different ureolytic $CaCO_3$-precipitating species were used in the present study: *Sporosarcina pasteurii* (ATCC 11859), *Sporosarcina aquimarina* (ATCC BAA-723), and *Sporosarcina newyorkensis*–a newly isolated microbe from the deep sea in offshore Japan. They were selected because they proliferate in different isolation environments: surface dry conditions, and shallow and deep sea, respectively. Thus, we emphasise that results presented herein did not necessarily represent a unique

group of $CaCO_3$-precipitating bacteria, but rather, organisms that proliferate and express the urease gene under the cultivation conditions used.

Both *S. pasteurii* and *S. aquimarina* were cultivated under sterile conditions in ATCC 1376 NH_4-YE medium in a shaking incubator (approximately 24 h at 30 °C and 200 rpm). Bacterial colonies were stored in an NH_4-YE agar plate in a refrigerator at 4 °C for up to a month before resuspending them in a fresh medium by the aforementioned process. Regarding *S. newyorkensis*, this was cultivated from a freeze-dried stock and resuspended under sterile conditions in ATCC 2216 Marine Broth medium in a shaking incubator (approximately 24 h at 30 °C and 200 rpm). Similarly, this strain was stored in MB agar plates in a refrigerator at 4 °C for up to a month. All three strains were harvested at an optical density of ~ 0.5, measured at a wavelength of 600 nm (OD_{600}). In addition, *S. pasteurii*–which is the most common soil bacterium used in geotechnical engineering applications–was also investigated under varying urea-$CaCl_2$ solution concentrations and initial bacterial densities (OD_{600}).

To ensure analogous reference conditions, all bacterial strains were cultivated under the same pressure and temperature–*i.e.* $P = P_{atm}$ and $T = 30\,°C$. It is acknowledged however that the environments from which the isolates were obtained could also have a selective influence on their viability. In this regard, the three bacterial strains were cultivated in static conditions during a 4-day period at varying temperatures–*i.e.* 4 °C, 15 °C, and 30 °C–, and pressures–*i.e.* 1 atm and 3 MPa–, and the bacterial density and urease activity were assessed.

Cementation solution

The cementation solution for MICP treatment was created using calcium chloride ($CaCl_2$), urea ($CO(NH_2)_2$) and Thermo Scientific Oxoid Nutrient Broth dissolved in deionised (DI) water. It was not autoclaved. $CaCO_3$ was precipitated *in vitro* in 14 mL test tubes at room temperature (each with a bacteria to cementation solution ratio of 1:2) and via the three different ureolytic soil bacteria described above. Precipitates were preserved after more than 30 days in the mother culture medium. Before further analysis, the solution was decanted, and solids collected and dried in an oven at 100° for 24 h to remove adsorbed water. Table S4 summarises the MICP treatment formulations and characterisation techniques used in the present study.

Biochemistry

Bacterial density: A Thermo Scientific Helios Zeta spectrophotometer was used to measure bacterial cell concentration–*i.e.* optical density–at a wavelength of 600 nm (OD_{600}). The degree of turbidity of the bacterial medium was directly related to the number of microorganisms present, both viable and dead cells. A higher turbidity therefore indicated a higher microbial cell mass. For the used apparatus, photometric accuracy decreased for $OD_{600} > 2.0$; in this case, the solution was diluted using a blank NH_4-YE or MB broth medium, and the obtained OD_{600} multiplied by the dilution factor.

Urease activity: The hydrolysis reaction of urea (Equation 1a) generates an increase in the overall electrical conductivity of the solution, linearly proportional to the concentration of active urease (Equation 2a). Urease activities of bacterial cells were thus determined by measuring the relative change in electrical conductivity when the bacterial solution was exposed to 1.11 M urea for a 5 min-duration. Subsequently, the rate of conductivity increase ($mS\,min^{-1}$) was converted to urea hydrolysis rate ($mM\,h^{-1}$) using Equation 2b. Finally, specific urease activity, defined as the urease activity by unit biomass, was calculated according to the following Equation 2c[28].

$$\text{Urea hydrolysed (mM)} = \text{Conductivity (mS)} \times 11.11 \tag{2a}$$

$$\text{Urease activity } (mM\,h^{-1}) = \frac{\Delta\text{Conductivity } (\mu S)}{\Delta t \text{ (min)}} \cdot \frac{10^{-3}\,mS}{1\,\mu S} \cdot \frac{60\,min}{1\,h} \cdot 11.11 \tag{2b}$$

$$\text{Specific urease activity } (mM\,h^{-1}\,OD_{600}^{-1}) = \frac{\text{Urease activity } (mM\,h^{-1})}{\text{Biomass } (OD_{600})} \tag{2c}$$

pH: pH was measured with a LAQUAtwin Compact pH Meter B-71X (range, $2.0 - 12.0$ pH, ± 0.1).

Aqueous calcium: Acqueous calcium was measured with a LAQUAtwin Compact Ca^{2+} Meter B-751 (range, $4 - 9900\,mg\,L^{-1}$).

Characterisation

Raman Spectroscopy: A confocal Horiba Jobin Yvon LabRAM 300 Raman spectrometer of 300 mm focal length at the Department of Earth Sciences, University of Cambridge was used to collect Raman spectra in the 100–1800 cm^{-1} spectral range. A holographic grating of 1800 $gr\,mm^{-1}$ coupled to a Peltier front illuminated CCD detector (1024×256 pixel in size) enabled a spectral resolution of $\sim 1\,cm^{-1}$. The excitation line at 532.05 nm was produced by a Laser Quantum Ventus 532 laser source focused on the sample using an Olympus LMPLFLN 50× long working distance objective. Collected Raman spectra were treated by PeakFit software (v4 for Win32)[62]. For each spectrum, the baseline was subtracted and peak features were

determined by least squares fitting to Voigt profiles for the Raman bands. Peak positions were calibrated against the measured excitation of a Ne light reference spectrum[63].

X-Ray Powder Diffraction (XRD): Measurements were performed at the Department of Earth Sciences, University of Cambridge using a Theta-theta Bruker D8 equipped with a copper sealed tube x-ray source producing Cu-Kα radiation at a wavelength of 1.5406 Å from a generator operating at 40 keV and 40 mA. Scanning rate was 0.03° 2Θ per minute from 15 to 50°. In addition, samples suspected to contain hydrated crystal phases (SA01-0.3 M, SP01-0.2 M-D, and SP01-0.2 M-ND) were also analysed from 3 to 50°. Only a broad hump in the range 4-9° 2Θ was consistently detected. Immediately after the acquisition a blank pattern was also acquired to exclude the possibility of noise from the sample holder. Diffractograms were interpreted using DIFFRAC.EVA software (v4.3.1)[64].

Thermal Analysis: Experiments were performed using a Mettler Toledo TGA/DSC 1 Star^e System analyser with a horizontal reaction chamber (Department of Engineering, University of Cambridge). Around 10-30 mg of sample were placed in a cylindrical 70 µL alumina crucible (ID 4.9 mm, depth 4 mm). The TGA furnace was constantly purged with 100 mL of Ar gas. Samples were heated from 50 °C to 1000 °C at a heating rate of 10 °/min in a stream of N_2 or Ar "reactive gas" provided directly above the sample with a flow rate of 50 mL min^{-1}. A baseline, obtained under the same conditions with an empty alumina crucible, was subtracted from the measured thermograms.

Mass spectroscopy (MS): The out-gas from TGA was directed to a quadrupole mass spectrometer, Hiden Analytical, HAL IV RC (Department of Engineering, University of Cambridge), to detect the presence of NH_3 ($m/z = 17$), H_2O ($m/z = 18$), NO_2 ($m/z = 30$), and CO_2 ($m/z = 44$). The measurements were performed using an SEM detector. The gas components were fragmented at 70 eV. To analyse a possible drift in time, a blank run obtained with an empty alumina crucible was performed after each experiment. The signal at $m/z = 17$ can be contributed both to NH3 and to [OH+], a fragment ion of water. The contribution of the [OH^-] ion was evaluate as 20% of the $m/z = 18$ signal value, and extracted from the signal at $m/z = 17$. The remaining signal at $m/z = 17$ was assigned to ammonia. All MS signals were normalised to a baseline shift value obtained after each experiment from a blank run using an empty crucible. Results therefore refer to relative incremental yields rather than absolute intensity values *per se*. The advantage of this was to be able to compare all exhaust gases using a single plot, allowing for thermal decomposition sequences to be unequivocally identified. The only exception was CO_2, plotted on its own intensity axis because its relative yield was considerably higher than that of the other products–understandable given that all of the analysed precipitates were carbonates. Therefore, where discussion warranted, zoomed in plots of the range of temperatures of interest showing the CO_2 yield with respect to the other products in the group were presented.

Scanning Electron Microscopy (SEM): Images of precipitates were obtained using a Phenom Pro Generation 5 (Department of Engineering, University of Cambridge). To observe the internal structure, epoxy casts of precipitates were made through the epoxy vacuum cast-embedding technique. Each mould was then cut to expose a fresh surface and polished using progressively finer grades of silicon carbide (SiC) paper (Grit 180-4000) and polishing alumina (1 and 0.3 µm). To observe the morphology, precipitates were dispersed onto a carbon adhesive-coated aluminium SEM mount and settled with a short burst of air. All samples were uncoated and images were acquired under backscattered scanning electron microscopy mode (SEM BSE) at a maximum resolution of 2048×2176 pixels.

References

1. Stocks-Fischer, S., Galinat, J. K. & Bang, S. S. Microbiological precipitation of CaCO3. *Soil Biol. Biochem.* **31**, 1563–1571, DOI: 10.1016/S0038-0717(99)00082-6 (1999).

2. Mitchell, A. C. & Ferris, F. G. The Influence of Bacillus pasteurii on the Nucleation and Growth of Calcium Carbonate. *Geomicrobiol. J.* **23**, 213–226, DOI: 10.1080/01490450600724233 (2006).

3. Warren, L. A., Mauri, P. A., Parmar, N. & Ferris, F. G. Microbially Mediated Calcium Carbonate Precipitation: Implications for Interpreting Calcite Precipitation and for Solid-Phase Capture of Inorganic Contaminants. *Geomicrobiol. J.* **18**, 93–115, DOI: 10.1080/01490450151079833 (2001).

4. Weiner, S. & Addadi, L. Design strategies in mineralized biological materials. *J. Mater. Chem.* **7**, 689–702, DOI: 10.1039/A604512J (1997).

5. Hammes, F., Boon, N., de Villiers, J., Verstraete, W. & Siciliano, S. D. Strain-Specific Ureolytic Microbial Calcium Carbonate Precipitation. *Appl. Environ. Microbiol.* **69**, 4901–4909, DOI: 10.1128/AEM.69.8.4901-4909.2003 (2003).

6. Burgos-Cara, A., V. Putnis, C., Rodriguez-Navarro, C. & Ruiz-Agudo, E. Hydration Effects on the Stability of Calcium Carbonate Pre-Nucleation Species. *Minerals* **7**, 126, DOI: 10.3390/min7070126 (2017).

7. Van Paassen, L. A. *Biogrout (ground improvement by microbially induced carbonate precipitation).* Ph.D. thesis, Delft University of Technology (2009).

8. Al Qabany, A. & Soga, K. Effect of chemical treatment used in MICP on engineering properties of cemented soils. *G@ACUTEACCENT@eotechnique* **63**, 331–339, DOI: 10.1680/geot.SIP13.P.022 (2013).

9. Montoya, B. & Dejong, J. Stress-Strain Behavior of Sands Cemented by Microbially Induced Calcite Precipitation. *J. Geotech. Geoenvironmental Eng.* **141**, 4015019, DOI: 10.1061/(ASCE)GT.1943-5606.0001302 (2015).

10. Terzis, D., Bernier-Latmani, R. & Laloui, L. Fabric characteristics and mechanical response of bio-improved sand to various treatment conditions. *Géotechnique Lett.* **6**, 50–57, DOI: 10.1680/jgele.15.00134 (2016).

11. Jiang, N.-J. & Soga, K. The applicability of microbially induced calcite precipitation (MICP) for internal erosion control in gravel-sand mixtures. *G@ACUTEACCENT@eotechnique* **67**, 42–55, DOI: 10.1680/jgeot.15.P.182 (2017).

12. Falini, G. Crystallization of calcium carbonates in biologically inspired collagenous matrices. *Int. J. Inorg. Mater.* **2**, 455–461, DOI: 10.1016/S1466-6049(00)00040-4 (2000).

13. Falini, G., Albeck, S., Weiner, S. & Addadi, L. Control of Aragonite or Calcite Polymorphism by Mollusk Shell Macromolecules. *Science* **271**, 67–69, DOI: 10.1126/science.271.5245.67 (1996).

14. Rodriguez-Navarro, C., Jimenez-Lopez, C., Rodriguez-Navarro, A., Gonzalez-Muñoz, M. T. & Rodriguez-Gallego, M. Bacterially mediated mineralization of vaterite. *Geochimica et Cosmochimica Acta* **71**, 1197–1213, DOI: 10.1016/j.gca.2006.11.031 (2007).

15. Raz, S., Testeniere, O., Hecker, A., Weiner, S. & Luquet, G. Stable Amorphous Calcium Carbonate Is the Main Component of the Calcium Storage Structures of the Crustacean Orchestia cavimana. *The Biol. bulletin* **203**, 269–274, DOI: 10.2307/1543569 (2003).

16. Kim, Y.-Y. *et al.* An artificial biomineral formed by incorporation of copolymer micelles in calcite crystals. *Nat. Mater.* **10**, 890 (2011).

17. Rae Cho, K. *et al.* Direct observation of mineral–organic composite formation reveals occlusion mechanism. *Nat. Commun.* **7**, 10187 (2016).

18. Kitamura, M. Crystallization and Transformation Mechanism of Calcium Carbonate Polymorphs and the Effect of Magnesium Ion. *J. Colloid Interface Sci.* **236**, 318–327, DOI: 10.1006/jcis.2000.7398 (2001).

19. Zou, Z. *et al.* A hydrated crystalline calcium carbonate phase: Calcium carbonate hemihydrate. *Science* **363**, 396–400, DOI: 10.1126/science.aav0210 (2019).

20. Tlili, M. *et al.* Characterization of CACO3 hydrates by micro-Raman spectroscopy. *J. Raman Spectrosc.* **33**, 10–16, DOI: 10.1002/jrs.806 (2002).

21. Ogino, T., Suzuki, T. & Sawada, K. The formation and transformation mechanism of calcium carbonate in water. *Geochimica et Cosmochimica Acta* **51**, 2757–2767, DOI: 10.1016/0016-7037(87)90155-4 (1987).

22. Sheng Han, Y., Hadiko, G., Fuji, M. & Takahashi, M. Crystallization and transformation of vaterite at controlled pH. *J. Cryst. Growth* **289**, 269–274, DOI: 10.1016/j.jcrysgro.2005.11.011 (2006).

23. Kralj, D., Brečević, L. & Kontrec, J. Vaterite growth and dissolution in aqueous solution III. Kinetics of transformation. *J. Cryst. Growth* **177**, 248–257, DOI: 10.1016/S0022-0248(96)01128-1 (1997).

24. Zhou, G.-t., Yao, Q.-Z., Fu, S.-Q. & Guan, Y.-b. Controlled crystallization of unstable vaterite with distinct morphologies and their polymorphic transition to stable calcite. *Eur. J. Mineral.* **22**, 259–269, DOI: 10.1127/0935-1221/2009/0022-2008 (2010).

25. Shen, Q. *et al.* Properties of Amorphous Calcium Carbonate and the Template Action of Vaterite Spheres. *The J. Phys. Chem. B* **110**, 2994–3000, DOI: 10.1021/jp055063o (2006).

26. White, W. B. Thermodynamic equilibrium , kinetics , activation barriers , and reaction mechanisms for chemical reactions in Karst Terrains. *Environ. Geol.* **30**, DOI: https://doi.org/10.1007/s002540050131 (1997).

27. Lioliou, M. G., Paraskeva, C. A., Koutsoukos, P. G. & Payatakes, A. C. Heterogeneous nucleation and growth of calcium carbonate on calcite and quartz. *J. Colloid Interface Sci.* **308**, 421–428, DOI: 10.1016/j.jcis.2006.12.045 (2007).

28. Whiffin, V. S. *Microbial CaCO3 Precipitation for the Production of Biocement*. Ph.D. thesis, Murdor University, Western Australia (2004). DOI: http://researchrepository.murdoch.edu.au/399/2/02Whole.pdf.

29. Yoneda, J. *et al.* Mechanical behavior of hydrate-bearing pressure-core sediments visualized under triaxial compression. *Mar. Petroleum Geol.* **66**, 451–459, DOI: 10.1016/j.marpetgeo.2015.02.028 (2015).

30. Gonzalez-Muñoz, M., Martinez-Ruiz, F., Morcillo, F., Martin-Ramos, J. & Paytan, A. Precipitation of barite by marine bacteria: A possible mechanism for marine barite formation. *Geology* **40**, 675–678, DOI: 10.1130/G33006.1 (2012).

31. Rodriguez-Blanco, J. D., Shaw, S. & Benning, L. G. How to make 'stable' ACC: protocol and preliminary structural characterization. *Mineral. Mag.* **72**, 283–286, DOI: 10.1180/minmag.2008.072.1.283 (2008).

32. Demény, A. *et al.* Formation of amorphous calcium carbonate in caves and its implications for speleothem research. *Sci. Reports* **6**, 39602, DOI: 10.1038/srep39602 (2016).

33. Farhadi-Khouzani, M., Chevrier, D. M., Zhang, P., Hedin, N. & Gebauer, D. Water as the Key to Proto-Aragonite Amorphous CaCO 3. *Angewandte Chemie - Int. Ed.* **55**, 8117–8120, DOI: 10.1002/anie.201603176 (2016).

34. Rodriguez-Navarro, C., Elert, K. & Ševčík, R. Amorphous and crystalline calcium carbonate phases during carbonation of nanolimes: implications in heritage conservation. *CrystEngComm* **18**, 6594–6607, DOI: 10.1039/C6CE01202G (2016).

35. Krishnamurti, D. The raman spectrum of calcite and its interpretation. *Proc. Indian Acad. Sci. - Sect. A* **46**, 183–202, DOI: 10.1007/BF03045968 (1957).

36. Farsang, S., Facq, S. & Redfern, S. Raman modes of carbonate minerals as pressure and temperature gauges up to 6 GPa and 500°C. *Am. Mineral.* DOI: 10.2138/am-2018-6442 (2018).

37. Xu, S. & Wu, P. Monodisperse spherical CaCO3 superstructure self-assembled by vaterite lamella under control of regenerated silk fibroin via compressed CO2. *CrystEngComm* **15**, 5179–5188, DOI: 10.1039/C3CE40181B (2013).

38. Buczynski, C. & Chafetz, H. S. Habit of bacterially induced precipitates of calcium carbonate and the influence of medium viscosity on mineralogy. *J. Sedimentary Res.* **61**, 226–233, DOI: 10.1306/D42676DB-2B26-11D7-8648000102C1865D (1991).

39. Chekroun, K. B. *et al.* Precipitation and Growth Morphology of Calcium Carbonate Induced by Myxococcus Xanthus: Implications for Recognition of Bacterial Carbonates. *J. Sedimentary Res.* **74**, 868–876, DOI: 10.1306/050504740868 (2004).

40. Rautaray, D., Ahmad, A. & Sastry, M. Biosynthesis of CaCO 3 Crystals of Complex Morphology Using a Fungus and an Actinomycete. *J. Am. Chem. Soc.* **125**, 14656–14657, DOI: 10.1021/ja0374877 (2003).

41. Sondi, I. & Matijević, E. Homogeneous precipitation of calcium carbonates by enzyme catalyzed reaction. *J. Colloid Interface Sci.* **238**, 208–214, DOI: 10.1006/jcis.2001.7516 (2001).

42. Simmonds, P. G., Medley, E. E., Ratcliff, M. A. & Shulman, G. P. Thermal decomposition of aliphatic monoaminomonocarboxylic acids. *Anal. Chem.* **44**, 2060–2066, DOI: 10.1021/ac60320a040 (1972).

43. Jie, L. *et al.* The investigation of thermal decomposition pathways of phenylalanine and tyrosine by TG–FTIR. *Thermochimica Acta* **467**, 20–29, DOI: 10.1016/j.tca.2007.10.014 (2008).

44. Ratcliff, M. A., Medley, E. E. & Simmonds, P. G. Pyrolysis of amino acids. Mechanistic considerations. *The J. Org. Chem.* **39**, 1481–1490, DOI: 10.1021/jo00924a007 (1974).

45. Heveran, C. M. *et al.* Engineered Ureolytic Microorganisms Can Tailor the Morphology and Nanomechanical Properties of Microbial-Precipitated Calcium Carbonate. *Sci. Reports* **9**, 14721, DOI: 10.1038/s41598-019-51133-9 (2019).

46. Rodriguez-Blanco, J. D., Sand, K. K. & Benning, L. G. ACC and Vaterite as Intermediates in the Solution-Based Crystallization of CaCO3. In Van Driessche, A. E. S., Kellermeier, M., Benning, L. G. & Gebauer, D. (eds.) *New Perspectives on Mineral Nucleation and Growth: From Solution Precursors to Solid Materials*, 93–111, DOI: 10.1007/978-3-319-45669-0{_}5 (Springer International Publishing, Cham, 2017).

47. Levi-Kalisman, Y., Raz, S., Weiner, S., Addadi, L. & Sagi, I. X-Ray absorption spectroscopy studies on the structure of a biogenic "amorphous" calcium carbonate phase. *J. Chem. Soc. Dalton Transactions* 3977–3982, DOI: 10.1039/B003242P (2000).

48. Koga, N. & Yamane, Y. Thermal behaviors of amorphous calcium carbonates prepared in aqueous and ethanol media. *J. Therm. Analysis Calorim.* **94**, 379–387, DOI: 10.1007/s10973-008-9110-3 (2008).

49. Beuvier, T. *et al.* Synthesis of hollow vaterite CaCO3 microspheres in supercritical carbon dioxide medium. *J. Mater. Chem.* **21**, 9757–9761, DOI: 10.1039/C1JM10770D (2011).

50. Takahashi, K. *et al.* Formation of 6-, 7- or 8-membered ring intra-side-chain NHO hydrogen bond toward Ca-binding oxyanion in poly(allylaminocarboxylate) ligands stabilizes CaCO3 vaterite crystals. *J. Cryst. Growth* **263**, 552–563, DOI: https://doi.org/10.1016/j.jcrysgro.2003.11.112 (2004).

51. Ueyama, N., Takahasi, K., Onoda, A., Okamura, T.-a. & Yamamoto, H. Tight binding of poly(carboxylate) ligand to calcium carbonate with intramolecular NH…O hydrogen bond. *Macromol. Symp.* **186**, 129–134, DOI: 10.1002/1521-3900(200208)186:1<129::AID-MASY129>3.0.CO;2-F (2002).

52. Štajner, L. *et al.* The effect of different amino acids on spontaneous precipitation of calcium carbonate polymorphs. *J. Cryst. Growth* **486**, 71–81, DOI: 10.1016/j.jcrysgro.2018.01.023 (2018).

53. Aizenberg, J., Addadi, L., Weiner, S. & Lambert, G. Stabilization of amorphous calcium carbonate by specialized macromolecules in biological and synthetic precipitates. *Adv. Mater.* **8**, 222–226, DOI: 10.1002/adma.19960080307 (1996).

54. Jaenicke, R. & Bohm, G. The stability of proteins in extreme environments. Current opinion in structural biology. *Curr. Opin. Struct. Biol.* **8**, 738–748 (1998).

55. Razvi, A. & Scholtz, J. M. Lessons in stability from thermophilic proteins. *Protein Sci.* **15**, 1569–1578, DOI: 10.1110/ps.062130306 (2006).

56. Matsumura, P., Keller, D. M. & Marquis, R. E. Restricted pH ranges and reduced yields for bacterial growth under pressure. *Microb. Ecol.* **1**, 176–189, DOI: 10.1007/BF02512388 (1974).

57. Kaneshiro, S. M. & Clark, D. S. Pressure effects on the composition and thermal behavior of lipids from the deep-sea thermophile Methanococcus jannaschii. *J. Bacteriol.* **177**, 3668–3672, DOI: 10.1128/jb.177.13.3668-3672.1995 (1995).

58. Kumar, P. & Libchaber, A. Pressure and Temperature Dependence of Growth and Morphology of Escherichia coli: Experiments and Stochastic Model. *Biophys. J.* **105**, 783–793, DOI: 10.1016/j.bpj.2013.06.029 (2013).

59. Yang, P., O'Donnell, S., Hamdan, N., Kavazanjian, E. & Neithalath, N. 3D DEM Simulations of Drained Triaxial Compression of Sand Strengthened Using Microbially Induced Carbonate Precipitation. *Int. J. Geomech.* **17**, 04016143, DOI: 10.1061/(ASCE)GM.1943-5622.0000848 (2017).

60. Feng, K., Montoya, B. M. & Evans, T. M. Discrete element method simulations of bio-cemented sands. *Comput. Geotech.* **85**, 139–150, DOI: https://doi.org/10.1016/j.compgeo.2016.12.028 (2017).

61. Yang, Z. X., Yang, J. & Wang, L. Z. On the influence of inter-particle friction and dilatancy in granular materials: a numerical analysis. *Granul. Matter* **14**, 433–447, DOI: 10.1007/s10035-012-0348-x (2012).

62. SigmaPlot. PeakFit - The Automatic Choice for Spectroscopy, Chromatography and Electrophoresis.

63. Saloman, E. B. & Sansonetti, C. J. Wavelengths, Energy Level Classifications, and Energy Levels for the Spectrum of Neutral Neon. *J. Phys. Chem. Ref. Data* **33**, 1113–1158, DOI: 10.1063/1.1797771 (2004).

64. EVA (Bruker). DIFFRAC.SUITE EVA.

65. Yoon, J. H. *et al.* Sporosarcina aquimarina sp. nov., a bacterium isolated from seawater in Korea, and transfer of Bacillus globisporus (Larkin and Stokes 1967), Bacillus psychrophilus (Nakamura 1984) and Bacillus pasteurii (Chester 1898) to the genus Sporosarcina as Sporosa. *Int. J. Syst. Evol. Microbiol.* **51**, 1079–1086, DOI: 10.1099/00207713-51-3-1079 (2001).

66. Ferrari, A. C., Robertson, J., Ferrari, A. C. & Robertson, J. Raman spectroscopy of amorphous, nanostructured, diamond-like carbon, and nanodiamond. *Philos. Transactions Royal Soc. London. Ser. A: Math. Phys. Eng. Sci.* **362**, 2477–2512, DOI: 10.1098/rsta.2004.1452 (2004).

67. Chan, Q. H. S., Zolensky, M. E., Bodnar, R. J., Farley, C. & Cheung, J. C. H. Investigation of organo-carbonate associations in carbonaceous chondrites by Raman spectroscopy. *Geochimica et Cosmochimica Acta* **201**, 392–409, DOI: https://doi.org/10.1016/j.gca.2016.10.048 (2017).

68. Beny-Bassez, C. & Rouzaud, J.-N. Characterization of Carbonaceous Materials by Correlated Electron and Optical Microscopy and Raman Microspectroscopy. *Scanning Electron Microsc.* **1985**, 119–132 (1985).

69. Tuinstra, F. & Koenig, J. L. Raman Spectrum of Graphite. *The J. Chem. Phys.* **53**, 1126–1130, DOI: 10.1063/1.1674108 (1970).

70. Wang, Y., Alsmeyer, D. C. & McCreery, R. L. Raman spectroscopy of carbon materials: structural basis of observed spectra. *Chem. Mater.* **2**, 557–563, DOI: 10.1021/cm00011a018 (1990).

71. Henry, D. G., Jarvis, I., Gillmore, G., Stephenson, M. & Emmings, J. F. International Journal of Coal Geology Assessing low-maturity organic matter in shales using Raman spectroscopy : E ff ects of sample preparation and operating procedure. **191**, 135–151, DOI: 10.1016/j.coal.2018.03.005 (2018).

72. Schmidt Mumm, A. & İnan, S. Microscale organic maturity determination of graptolites using Raman spectroscopy. *Int. J. Coal Geol.* **162**, 96–107, DOI: 10.1016/j.coal.2016.05.002 (2016).

73. Chen, S., Wu, D., Liu, G. & Sun, R. Raman spectral characteristics of magmatic-contact metamorphic coals from Huainan Coalfield, China. *Spectrochimica Acta Part A: Mol. Biomol. Spectrosc.* **171**, 31–39, DOI: 10.1016/j.saa.2016.07.032 (2017).

74. Moldoveanu, S. C. Pyrolysis of Amines and Imines. In *Pyrolysis of Organic Molecules*, 327–347, DOI: 10.1016/B978-0-444-64000-0.00008-1 (Elsevier, 2019).

75. Raz, S., Hamilton, P., Wilt, F., Weiner, S. & Addadi, L. The Transient Phase of Amorphous Calcium Carbonate in Sea Urchin Larval Spicules: The Involvement of Proteins and Magnesium Ions in Its Formation and Stabilization. *Adv. Funct. Mater.* **13**, 480–486, DOI: 10.1002/adfm.200304285 (2003).

76. Mann, S., Heywood, B. R., Rajam, S. & Birchall, J. D. Controlled crystallization of CaCO3 under stearic acid monolayers. *Nature* **334**, 692–695, DOI: 10.1038/334692a0 (1988).

77. Cox, G. B., Jans, D. A., Fimmel, A. L., Gibson, F. & Hatch, L. Hypothesis the mecanism of ATP synthase conformational change by rotation of the b-subunit. *Biochimica et Biophys. Acta (BBA) - Rev. on Bioenerg.* **768**, 201–208, DOI: https://doi.org/10.1016/0304-4173(84)90016-8 (1984).

78. Ito, M. *et al.* MotPS is the stator-force generator for motility of alkaliphilic Bacillus, and its homologue is a second functional Mot in Bacillus subtilis. *Mol. Microbiol.* **53**, 1035–1049, DOI: 10.1111/j.1365-2958.2004.04173.x (2004).

79. Jahns, T. Ammonium / urea-dependent generation of a proton electrochemical potential and synthesis of ATP in Bacillus pasteurii. *J. Bacteriol.* **178**, 403–409 (1996).

80. Peng, X. & Jones, B. Patterns of biomediated CaCO3 crystal bushes in hot spring deposits. *Sedimentary Geol.* **294**, 105–117, DOI: 10.1016/j.sedgeo.2013.05.009 (2013).

81. Dominguez Bella, S. & Garcia-Ruiz, J. Textures in induced morphology crystal aggregates of CaCO3: Sheaf of wheat morphologies. *J. Cryst. Growth* **79**, 236–240, DOI: 10.1016/0022-0248(86)90444-6 (1986).

Acknowledgements

The authors would like to thank John Chandler, Kristian Pether, Mark Smith, and Chris McGinnie for facilitating the experiments; Dr Giulio I. Lampronti and Len Howlett for their assistance with XRD and SEM analysis, respectively; Dr Stuart Scott for lending he TGA-MS equipment; and Dr Rod Lynch for reviewing the manuscript. The authors would also like to acknowledge the EPSRC Centre for Doctoral Training in Future Infrastructure and Built Environment at the University of Cambridge (EPSRC grant reference number EP/L016095/1). This study was conducted as part of the activity of the Research Consortium for Methane Hydrate Resources in Japan [MH21 Research Consortium] as planned by the Ministry of Economy, Trade, and Industry (METI), Japan. We would like to express our sincere thanks to the crew of D/V Chikyu for the 2012 JOGMEC/JAPEX pressure coring operation.

Author contributions statement

A.C.S, S.K.H. and T.H. conceived experimental program. T.H. isolated *S. newyorkensis*. A.C.S. and T.H. cultivated the three bacterial strains, performed *in vitro* precipitation, and monitored chemical evolution. S.A.T.R. advised on the Raman spectroscopy collection program and data interpretation. A.C.S. and S.F. collected the Raman spectra, and analysed and interpreted the results. E.M. conducted MS analyses and helped A.C.S. with the acquisition and interpretation of TG-MS results. A.C.S. performed the XRD analyses and SEM images. T.H. planned and performed the pressure-temperature cultivation experiments, and A.C.S. analysed and interpreted the results. K.S. facilitated the collaboration between A.C.S, S.K.H, and T.H. A.C.S coordinated the collaboration and wrote the manuscript with the help of co-authors. All authors reviewed the manuscript.

Additional information

Competing interests: The authors declare no competing financial interests.
Supplementary information accompanies this paper.
Correspondence and requests for materials should be addressed to A.C.S.

Supplementary material

This document includes:

- Supplementary figures
- Supplementary tables
- Supplementary discussion

Supplementary figures

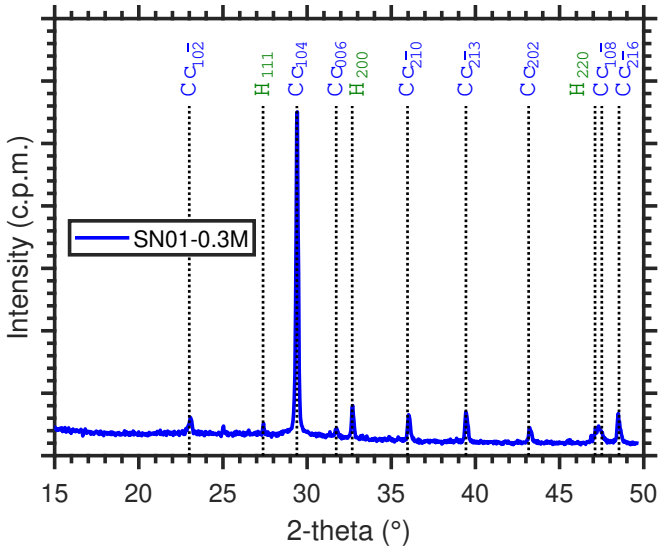

Figure S1. XRD pattern of SN01-0.3 M with *hkl* values of Bragg peaks indicated (Cu-Kα radiation, $\lambda = 1.5406$ Å). Cc, calcite; H, halite. Halite precipitation resulted from desiccating marine broth media used to cultivate the isolate and its presence was evidenced by the diffraction peaks at 27.41, 32.71, and 47.14° 2Θ.

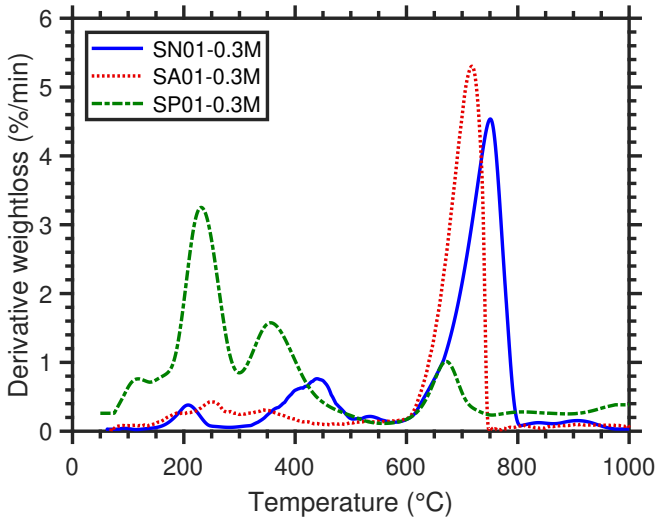

Figure S2. Derivatives of TGA curves in Figure 1b measured upon heating at a rate of 10 °C min^{-1}. SN01-0.3 M: Ar "reactive gas" flow rate 50 mL min^{-1}; SA01-0.3 M and SP01-0.3 M: N_2 "reactive gas" flow rate 50 mL min^{-1}.

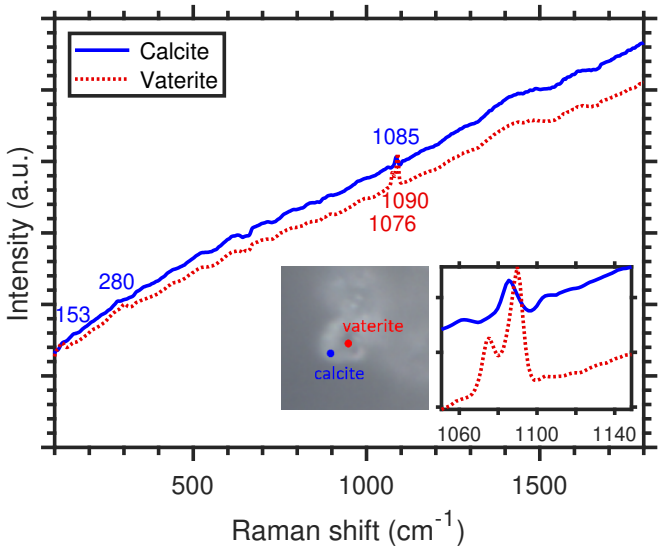

Figure S3. Raman spectra of polymorphic $CaCO_3$ crystal formed in the presence of *S. aquimarina* (SA01-0.3 M) with target collection points indicated in the optical microscopy image. Spectra showed that calcite weakened as the splitting of the ν_1 mode into two peaks became apparent, indicating the coexistence of calcite and vaterite within a "single crystal". This revealed that spectra that were thought to only correspond to calcite resulted from the superposition of both structures, but because of the large proportion of calcite relative to vaterite, the latter could only be inferred through the broadening of the ν_1 mode.

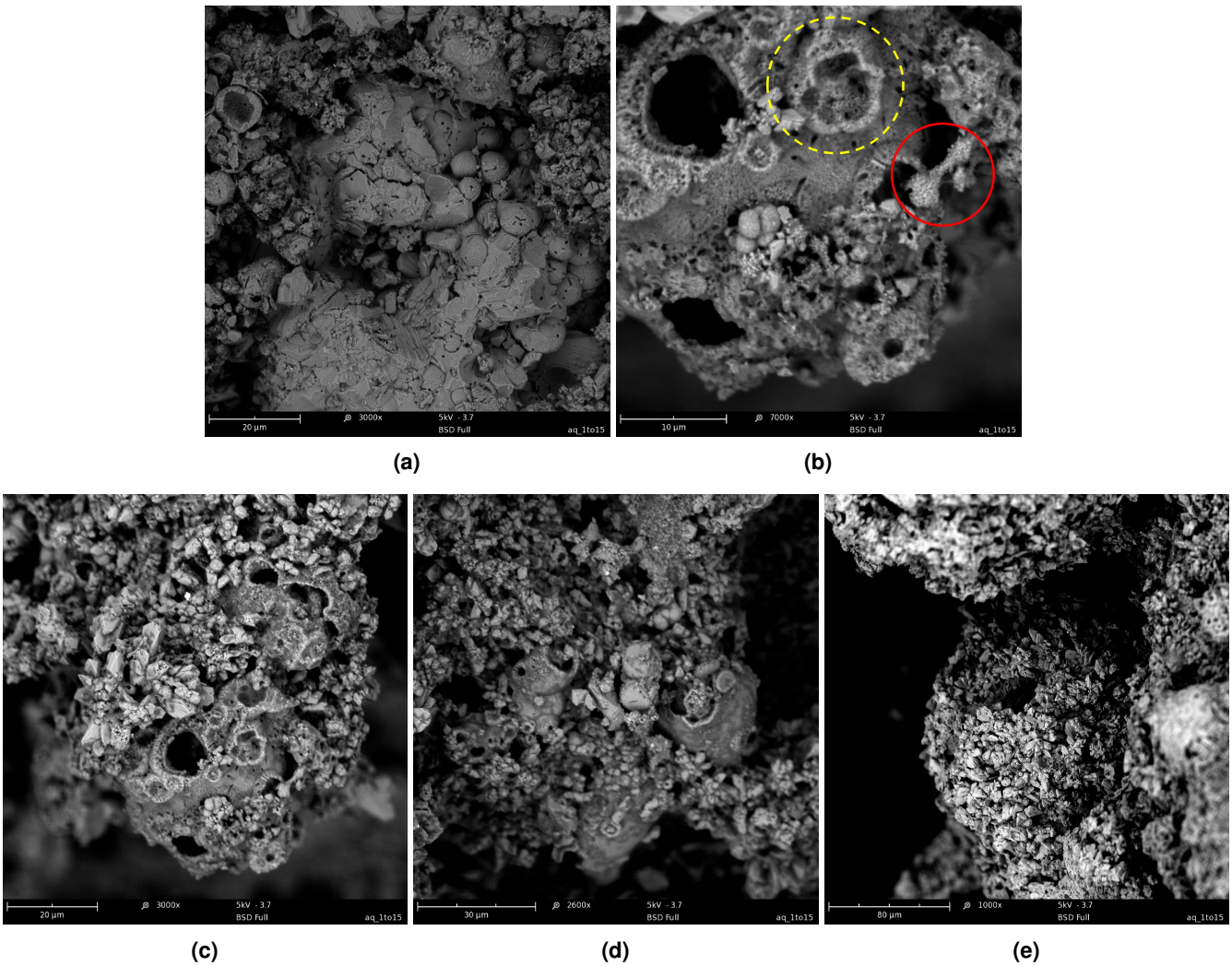

Figure S4. SEM BSE images of biotic precipitates formed in the presence of *S. aquimarina* (SA01-0.3 M) revealing the incorporation of the vaterite spherulites into the calcite crystals: (a) general overview showing vaterite spherulites overgrown by calcite crystals; (b) dumbbell shape precipitate associated with the initial stage of spherulite growth (red solid circle) and "crater"-like cavity formed post-vaterite dissolution (yellow dashed circle); (c) initial stage of calcite overgrowth; (d) filling in of cavities by advancing calcite precipitates; (e) spheroidal aggregate of calcite crystals with empty nucleus. It is clear that spherulites were gradually entrapped and, as incorporation continued, a cavity began to form around the perimeter of the spherulite. It is hypothesised, however, that cavities associated with larger spherulites persisted longer, but all would eventually either cover or be filled in by advancing calcite precipitates. Significantly, smaller "crater"-like cavities also appeared upon dissolution of smaller vaterite spherulites. These SEM images support the idea that vaterite close to the surface underwent a vaterite-calcite transition, *i.e.* calcite formed from vaterite.

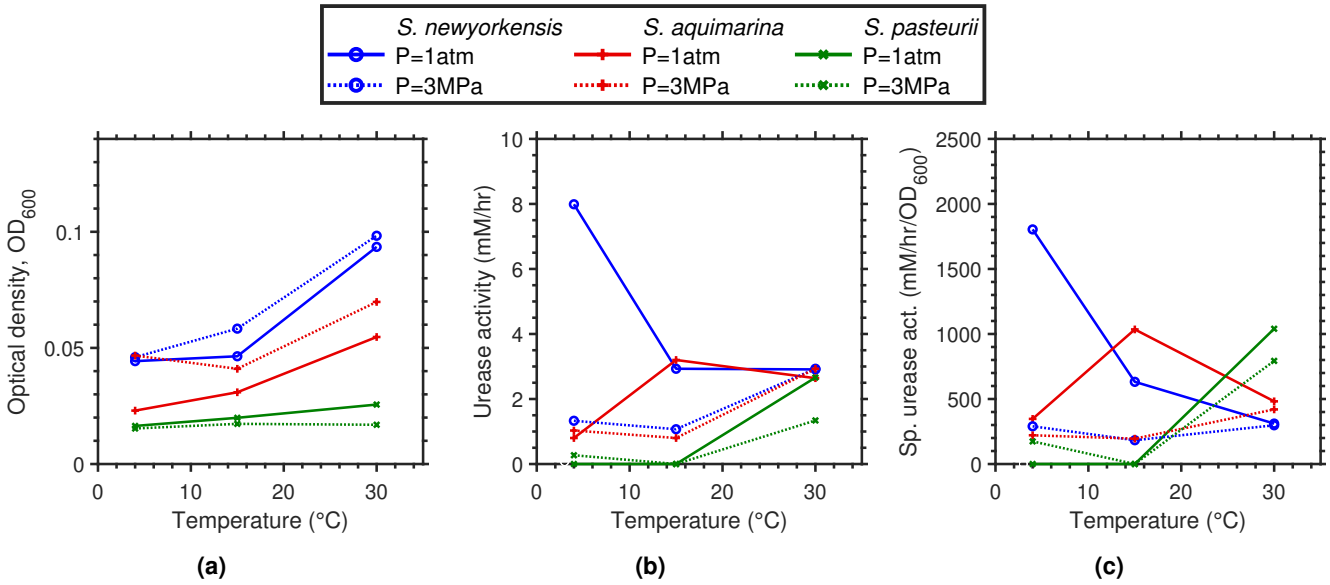

Figure S5. Pressure-temperature dependence after 1-day cultivation of: (a) bacterial density showing that OD_{600} increased with temperature. This effect was most pronounced between 15 and 30 °C, irrespective of pressure; and for *S. newyorkensis*, followed by *S. aquimarina* and *S. pasteurii*. This may be explained by a decrease in dissolved oxygen with increasing temperature. Indeed, an oxygen-limited environment would have prompted the growth of (facultative) anaerobic microorganisms–*i.e. S. newyorkensis* and *S. aquimarina*[65]; (b) urease activity and , (c) specific urease activity showing that changes due to pressure were only apparent at particular temperatures, which differed between bacterial strains. For *S. newyorkensis*, the urease activity drop with pressure was most significant at 4 °C, and the gap narrowed with increasing temperature. For *S. aquimarina*, the urease activity at 3 MPa only diverged from that at 1 atm at $T = 15$ °C, while this occurred at 30 °C for *S. pasteurii*. It is thus clear that urease activity was more sensitive to pressure at temperatures near those of the original isolation environment.

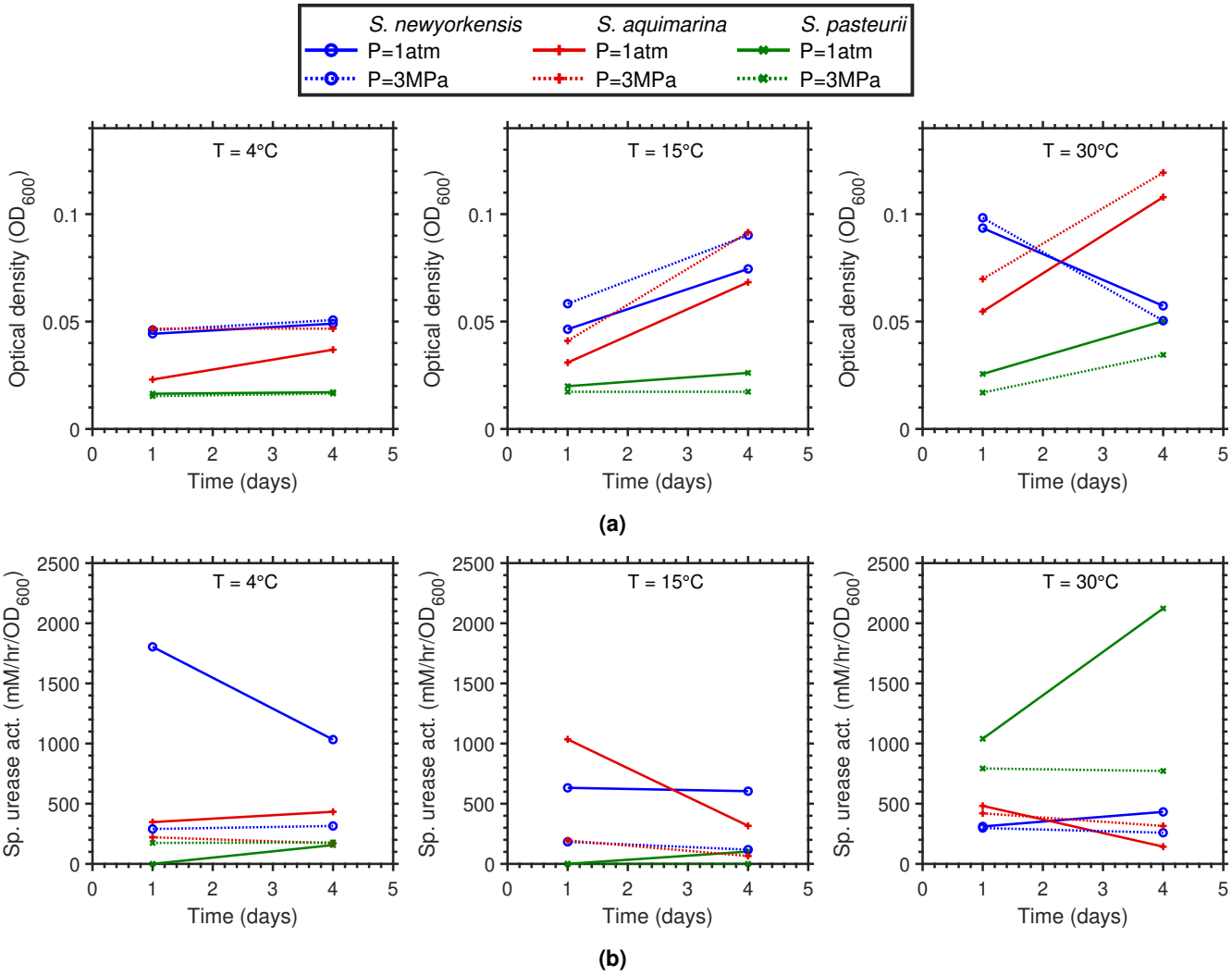

Figure S6. Pressure-temperature dependence during a 4-day cultivation of: (a) bacterial density, showing that in all cases temperature accelerated bacterial growth, while pressure had a much less pronounced effect. Over 4 days, *S. newyorkensis* only grew at 15 °C; *S. aquimarina*'s optimal growth temperature was 30 °C, although it also grew well at 15 °C; and *S. pasteurii* only grew at 30 °C; and (b) showing a loss of specific urease activity with pressure for all three ureolytic microorganisms, suggesting that pressure potentiates inhibitory factors that affect the function of the urease enzyme. It is also clear that aside from pressure and temperature, time played an important role.

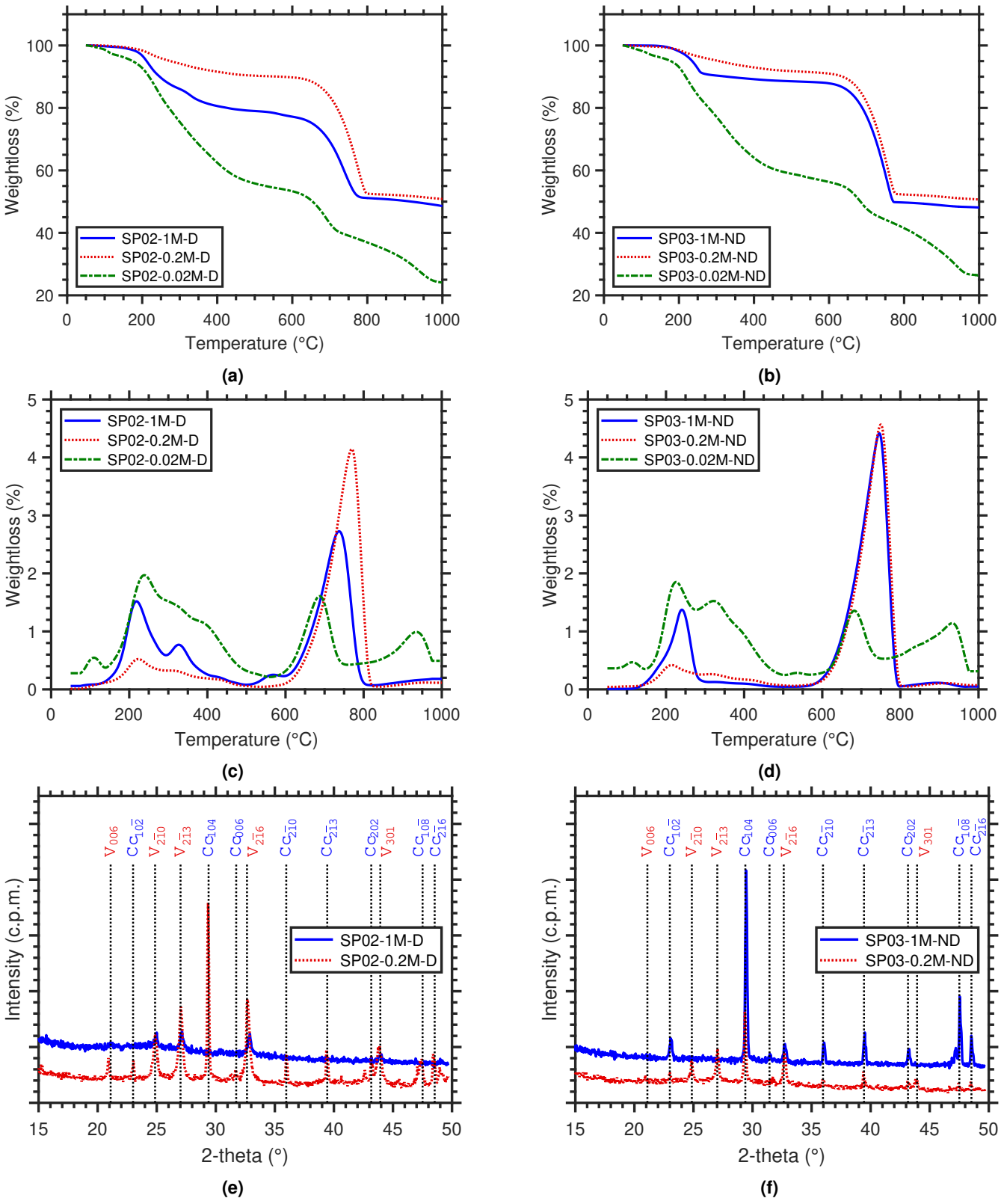

Figure S7. TG-DTG curves (heating rate 10 °C min^{-1}; N_2 "reactive gas" flow rate 50 mL min^{-1}) (a-d); and XRD pattern with *hkl* values of Bragg peaks indicated (Cu-Kα radiation, $\lambda = 1.5406$ Å) (e,f) of precipitates of *S. pasteurii* (see Table S4 for nomenclature). V, vaterite; Cc, calcite. TG-DTG analysis for SP01-0.02 M showed two peaks at high temperatures (690 and 930 °C) associated with the decarbonation of $CaCO_3$ and the pyrolysis of amino acids.

Supplementary discussion

XRD and Raman spectral characteristics of organic matter

XRD showed a broad hump with a maximum at $\sim 6.3°$ 2Θ associated with the presence of an amorphous material (Figure S8a). Immediately after the acquisition, a blank pattern was also acquired to exclude the possibility of noise from the sample holder.

A preliminary understanding was obtained through Raman spectroscopy (Figure S8b). Well-crystalline graphitic materials–*i.e.* consisting primarily of a crystalline C−C network–will always display a Graphite (G) band, corresponding to the stretching mode in both rings and chains of carbon atoms[66,68,69]. With increasing disorder, the additional Disorder (D) band appears due to a break in symmetry by the presence of edges or defects[70]. In fact, this is explained by introducing the "amorphization trajectory", a three stage model depicting the variation of the Raman G position and the D-to-G intensity ratio $R1 = I(D)/I(G)$ with increasing disorder[66]. As amorphization increases, there is an associated topological conversion of the C−C network, from rings to chains, ultimately making the $I(D)/I(G) = 0$ due to the absence of rings. Consequently, the appearance of D bands is attributed to the breathing mode of aromatic structures alone; thus, no rings, no D peak[66,68,69]. Aside from peak position and intensity, essential parameters used to characterise organic material include full width half maximum (FWHM), the ratio of band areas $RA1 = A(D)/A(G)$, and Raman band separation $RBS = \Delta_{G-D}$[71]. The following observations are reported in the literature regarding the Raman spectral parameters of organic material, listed in Table S2:

- *Peak position, RBS:* A limiting point for the G band has been suggested at 1600 cm^{-1}[66], and higher wavelengths are associated with an increasing abundance of distortion in the graphite structure[72]. Conversely, an upward shift of the position of the D band is reported with a decrease in size of the aromatic clusters, and thus decreasing amorphization[66,72,73]. Therefore, *RBS* decreases with increasing structural ordering.
- *FWHM:* The FWHM of the G band is a measure of disorder and increases continuously as the disorder increases[66]; this occurs with a concurrent decrease in intensity[72].
- *RA1* decreases with increasing structural ordering[73].
- The shoulder between the D and G bands increases with decreasing level of organisation[72].

Taken together, these results indicated the following about the precipitates of *S. newyorkensis* and *S. aquimarina*:

- The $CaCO_3$ crystal structure was composed of somewhat distorted carbonate groups.
- Presence of topologically disordered organic matter composed of aromatic molecules and amorphous carbon.
- Direct interactions between organic macromolecules, presumably from exopolymeric organic substances (EPS) or as a by-product from the bacterial activity, and the $CaCO_3$ crystal structure.
- The lower value of the Raman parameters *R*1, *RA*1, and *RBS* of *S. aquimarina* suggested a higher degree of structural ordering of the organic material.

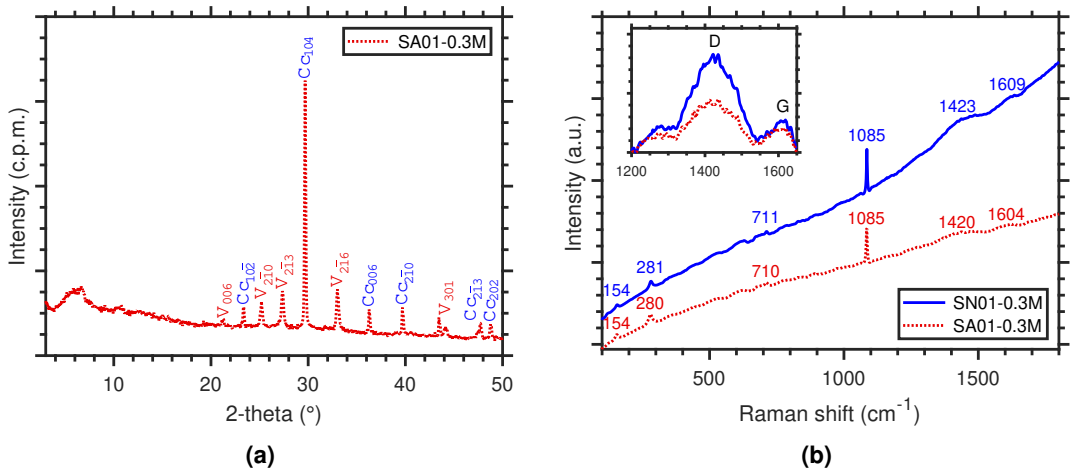

Figure S8. (a) XRD pattern for precipitates of *S. aquimarina* with *hkl* values of Bragg peaks indicated and showing a broad hump with a maximum at $\sim 6.3°$ 2Θ associated with the presence of an amorphous material. V, vaterite; Cc, calcite (Cu-Kα radiation, $\lambda = 1.5406$ Å). Immediately after the acquisition, a blank pattern was also acquired to exclude the possibility of noise from the sample holder. (b) Raman spectra of precipitates of *S. aquimarina* and *S. newyorkensis* showing the presence of a the D and G bands, known to move from 1581 cm^{-1} to *ca.* 1600 cm^{-1} during the first stage of the "amorphization trajectory"[66]. A G band is always expected in the presence of organic matter, regardless of the structural order[66,67]. In addition, the small peak at *ca.* 1420 cm^{-1}, potentially associated with a D band[67], further hinted to the presence of highly disordered carbonaceous materials.

Pyrolysis of amino acids

Pyrolysis of β-amino acids: The decomposition pathway for β-amino acids is one of deamination to yield unsaturated carboxylic acid and amine as intermediates. These decarboxylate and deaminate, respectively, during a secondary decomposition. Similar explanations can be used to account for the loss of water observed during TG-MS analysis of precipitates of *S. newyorkensis*. The presence of only a trace of water during the first stage suggested that water was primarily a consequence of pyrolysis of amino acids and not from crystallisation. In fact, pyrolysis of carboxylic acids has been reported to yield aldehydes and ketones proceeding an acyl radical. The presence of CO preceding the H_2O release between 600-800 °C lent some support to the transitory existence of this acyl radical[42]. This plausible route for the pyrolysis of amino acids in precipitates of *S. newyorkensis* is schematically shown in Figure S9a.

Primary decomposition of α-amino acids: Deamination was a primary, although minor, mode of decomposition, evidenced by the small NH_3 peak measured between 100-160 °C.[44] observed this during the pyrolysis of α-amino acids and attributed it to the existence of an intermediate (*i.e.* α-lactone) that subsequently decarbonylates, accounting for the formation of aldehydes (m/z = 18). While no CO was measured herein, the aldehyde formation provided partial evidence of this primary decomposition step.

Pyrolysis of amines: Previous studies suggest that the pyrolysis of amines can happen through the loss of hydrogen and formation of a nitrile via an imine intermediate, which is trapped through a condensation reaction that releases water[42,74]. This compounds are known to very stable to heating[74]. In addition, pyrolysis of amines can also occur with the cleavage of a C−C bond (α cleavage), evidenced by a base peak at $m/z = 30$ in primary amines spectra (Figure 3b). Finally, traces of CO_2 were detected between 300 °C and 600 °C, potentially indicating that imines were created by eliminating CO_2 through the pyrolysis of amino acids. Thus, the carboxyl group in the original compound was less stable than the imine group. These plausible routes for the pyrolysis of amino acids in precipitates of *S. aquimarina* are schematically shown in Figure S9b.

In conclusion, the composition of the amino acids present in precipitates of *S. newyorkensis* and *S. aquimarina* (Figure 3) was significantly different. This was evidenced by the almost total distinction between their primary modes of decomposition. While the amino acids in *S. aquimarina* underwent dehydration and decarboxylation with at most very minor deamination, the amino acids in *S. newyorkensis* produced ammonia as a major product. While the former was in agreement with presence α-amino acids, the latter corresponded to β-amino acids. Although this research was not able to ascertain the causes of this

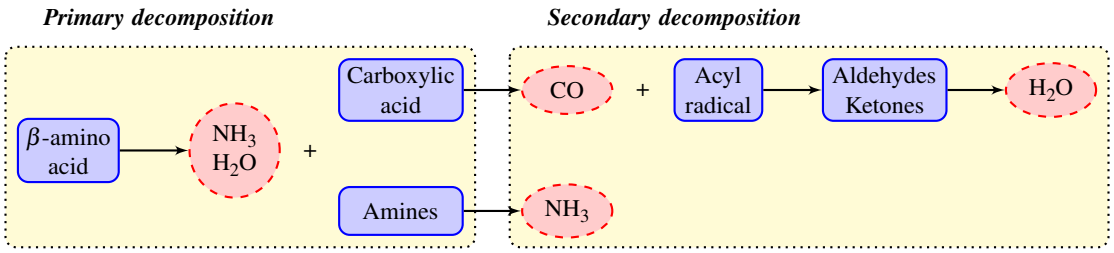

(a) *S. newyorkensis* (SN01-0.3 M)

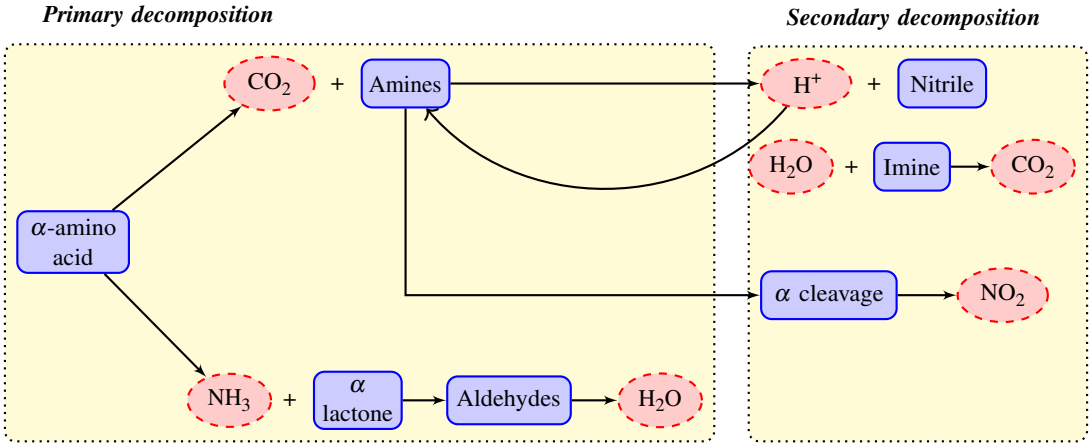

(b) *S. aquimarina* (SA01-0.3 M)

Figure S9. Plausible routes for pyrolysis of amino acids in $CaCO_3$ precipitates of *S. newyorkensis* and *S. aquimarina*.

(a) Overview of calcite crystals embedded in an organic matrix. Magnification: 1000×.

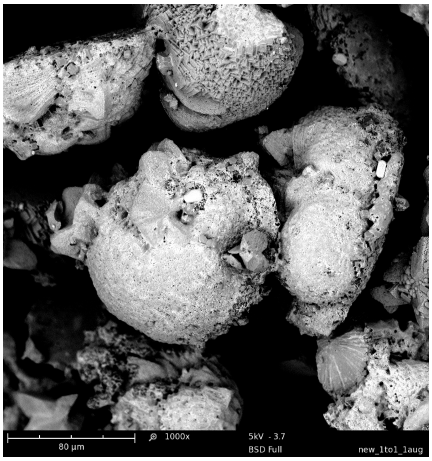

(b) Crystals with porous smooth surfaces and sharp edges.
Magnification: 1000×.

(c) Rhombic calcite crystals with beveled edges and corners.
Magnification: 3000×

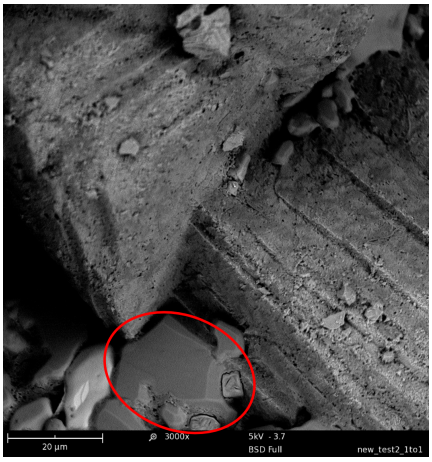

(d) Inter-grown and dodecahedral crystals with pentagonal faces. Magnification: 3000×.

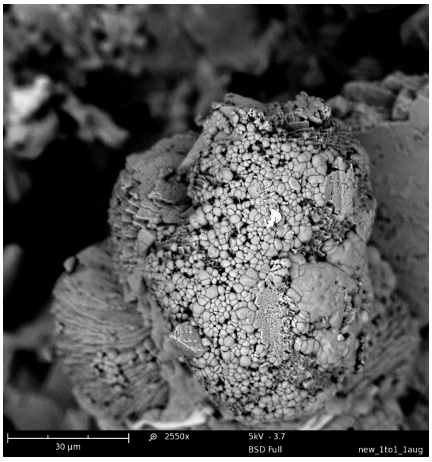

(e) Oval beads lying on top of calcite concentric branches.
Magnification: 2550×.

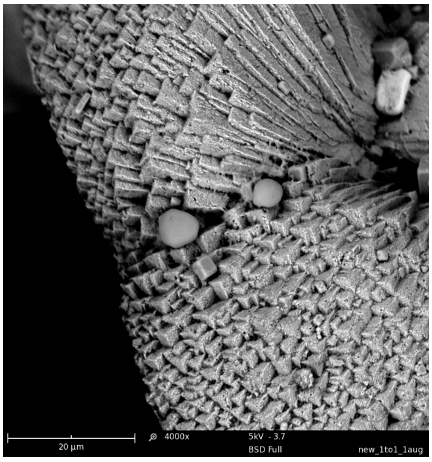

(f) Cluster of radiating lapillus crystals.
Magnification: 4000×.

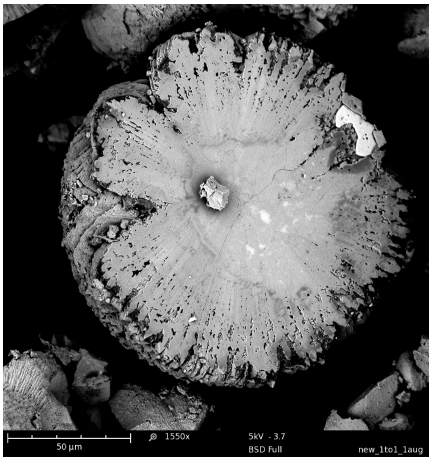

(g) Crystal flat base showing radiating inner structure. Magnification: 1550×.

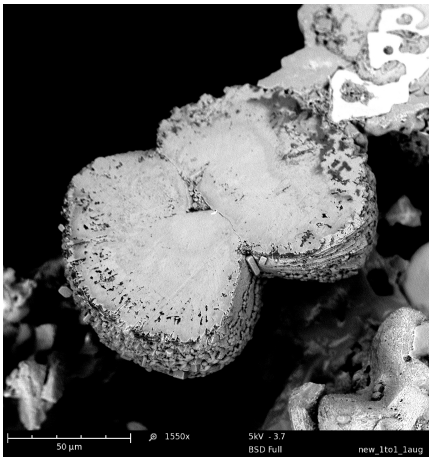

(h) Wheat-sheaf of crystals with starting signs of a hollow core. Magnification: 1550×.

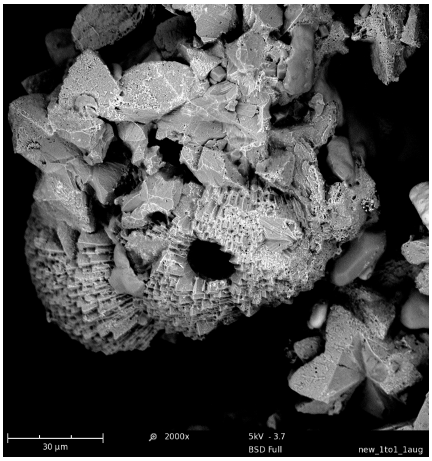

(i) Calcite crystals in outer part of radiating cluster with hollow core. Magnification: 2000×.

Figure S10. SEM BSE images of biotic precipitates of *S. newyorkensis* (SN01-0.3 M).

difference, they were most likely related to:

- Conformational modifications–*i.e.* changes in shape yielding structural fluctuations–used by different organisms to control the calcification process[75,76].
- Strain-specific urea hydrolysis metabolism processes yielding different organic by-products.
- Strain-specific extracellular polymeric substances (EPS) made of proteins which consist of different amino acid residues (extensively reviewed in[14]).

A well-established example of the first observation is the motility of *S. pasteurii*, which is related to cell's membrane potential. This bacterium hydrolyses urea to trigger the rotational torque of the flagella, driving the conformational changes that result in the generation of adenosine triphosphate (ATP)[77–79]. Hence, the polymorph structural information may rely heavily on understanding the function behind urea hydrolysis. Nonetheless, this was out of the scope of the stated objectives.

From these analyses it was then possible to qualitatively compare the morphological features of precipitates of *S. newyorkensis* (Figure S10) with those described for *S. aquimarina*. The difference was remarkable. As shown in Figure S10a, precipitates of *S. newyorkensis* were completely embedded in an organic matrix, making a continuous network that bridged all the crystalline units, and characterised by the juxtaposition of smooth faces and sharp edges (Figure S10b). Calcite–which was the only $CaCO_3$ polymorph present in specimen SN01-0.3 M (Figure S1)–was mainly observed in the form of inter-grown crystal clusters (Figure S10c). Occasionally, these were associated with dodecahedral crystals with pentagonal faces (Figure S10d). Very similar biomediated $CaCO_3$ morphologies have been found in hot spring deposits by[80].

While at first there was no recognisable pattern to the distribution of these crystalline units, a closer look revealed clear signs of concentric bands. In all cases, these consisted of elongated prisms with a thickness of *ca.* 5 µm emanating from a growth centre. Their surface textural organisation appeared both in beads of ~ 3 µm in diameter (Figure S10e) and lappilus (Figure S10f). In addition, flat bases characterised many of the clusters (Figure S10g-h), where a clear wheat-sheaf pattern was observed in the internal structure[81]. From this, it was hypothesised that clusters formed by radiating from a common nucleus. As growth continued, they separated (Figure S10h), creating hollow cores of approximately 15 µm (Figure S10i). Although the way this matrix functions is still not fully understood, these SEM images further reinforced the point that morphological features cannot be unambiguously used to identify biosignatures of bacterial activity.

Pyrolysis of ACC

Although mass spectra for these samples were unavailable, the above observations were confirmed by comparison with the MS pattern of specimen SP01-0.3 M (Figure S11). Some important insights into the thermal behaviour of ACC precipitated in the presence of *S. pasteurii* were thus obtained:

- The dehydration process proceeded via two separate weight loss steps, at *ca.* 80 and 220 °C, with the latter being most significant. The total weight loss in this transition was of about 15 wt%. This suggested the presence of α-amino acids, which underwent a primary, although minor, decomposition mode involving a double dehydration reaction yielding first a dipeptide and subsequently a diketopiperazine (DKP)[42–44]. In fact, the existence of a DKP intermediate during the decomposition of the amino acids provided an attractive explanation for the formation of CO between 350-600 °C.[43] suggested that a low yield of H_2O predicated a low yield of DKP, consequently decomposing into HCN and CO at lower temperatures than expected (400-500 °C rather than 700 °C). Thus, the low yield of H_2O preceding the CO release provided strong evidence for DKP involvement.
- Similar to precipitates of *S. aquimarina* (Figure S9b), the third weight loss was 5-6 wt% and occurred in the temperature range of 200-250 °C. This corresponded to a second primary decomposition of α-amino acids, which underwent decarboxylation with very minor deamination–as evidenced by the relative high yield of CO_2 compared to that of NH_3 shown in the zoomed in plot of Figure S11.
- Decarboxylation of α-amino acids yielded CO_2 and the formation of amines as major products. The subsequent condensation reaction of an aldehyde or ketone with these primary amines– evidenced by the continuous loss of water between 220-400 °C–potentially led to the creation of very thermally stable imines. The release of CO_2 at *ca.* 900 °C would thus indicate that the carboxyl group in the compound was less stable than the parent molecule[74]–rather than the decomposition of the imine *per se*.
- The weight loss at 740 °C (25 wt%) corresponded to the decomposition of $CaCO_3$ to CaO.

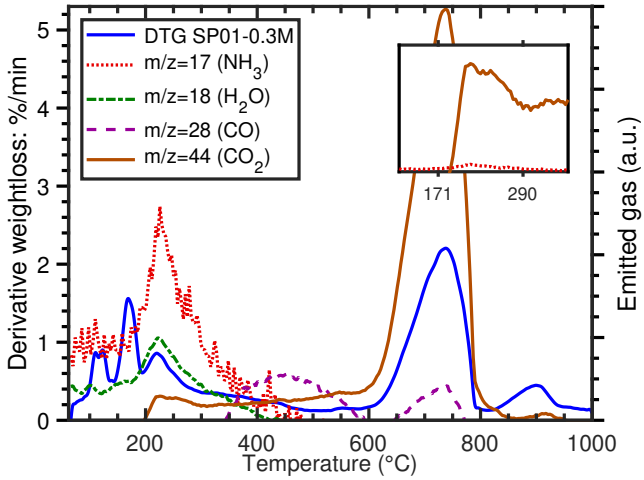

Figure S11. DTG and mass spectra of evolved gases measured from coupled TG-MS of $CaCO_3$ crystals formed in the presence of *S. pasteurii* (SP01-0.03 M) (heating rate 10 °C min^{-1}; Ar "reactive gas" flow rate 50 mL min^{-1}).

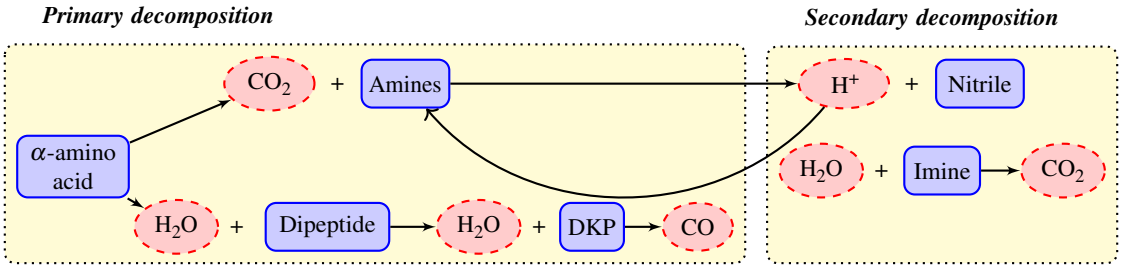

Figure S12. Plausible routes for pyrolysis of amino acids in $CaCO_3$ precipitates of *S. pasteurii* (SP01-0.03 M).

Supplementary tables

Assignment	Sample name[a], polymorph[b]		
	SN01-0.3 M	SA01-0.3 M	
	Cc	Cc	V
Lattice vibration	154	154 (155)[c]	-
Lattice vibration	281	280	-
In-plane bending, ν_4	711	710	-
Symmetric CO stretching, ν_1	1085	1085 (1086)	1076, 1090 (1088)
Graphite band, G	1609	1604	-

[a] Names describe bacterial strain initials, test number, and total concentration of $CaCl_2$.
[b] Cc, calcite; V, vaterite.
[c] Results from a second acquisition in parenthesis.

Table S1. Peak positions in the Raman spectra of *S. newyorkensis* (SN01-0.3 M) and *S. aquimarina* (SA01-0.3 M) precipitates and peak assignment to different vibration modes.

Sample name	Raman spectral parameters							
	Band	Position (cm^{-1})	FWHM (cm^{-1})	Intensity (a.u.)	Area (a.u.)	R1[a]	RA1[b]	RBS (cm^{-1})[c]
SN01-0.3 M	G	1609	60	521	3.3×10^4	3.1	7.6	186
	D	1423	146	1594	2.5×10^5			
SA01-0.3 M	G	1604	64	402	2.7×10^4	2.1	5.2	184
	D	1420	151	857	1.4×10^5			

[a] Ratio of Raman band height intensity: $R1 = I(D)/I(G)$[66].
[b] Ratio of Raman band areas: $RA1 = A(D)/A(G)$[73].
[c] Raman Band Separation: $RBS = \Delta_{G-D}$[72].

Table S2. Raman parameters of the Disorder (D) and Graphite (G) bands of *S. newyorkensis* (SN01-0.3 M) and *S. aquimarina* (SA01-0.3 M) used to determine the degree of organisation of the organic carbons.

m/z	Fragment	Possible chemical class
17	NH_3/OH^-	Amines
18	H_2O	Aldehydes, ketones
28	CO	Aromatic ethylethers, ethylesters, n-propylketones
30	NO_2	Aromatic NO_2
44	CO_2	Anhydrides

Table S3. Common fragments from molecular-ions emitted during MS.

Bacterial Strain	Sample name[a]	Cementation solution formulation[b]	Biochemistry				Characterisation			
			OD_{600}	UA: $mM\,h^{-1}$ (SUA: $mM\,h^{-1}\,OD_{600}^{-1}$)	pH	$c(Ca^{2+})$	RM	XRD	TGA	MS
S. newyorkensis	SN01-0.3 M	1:1 (0.3 M)	0.555	6.6 (118.9)	X	X	X	X	X	X
S. aquimarina	SA01-0.3 M	1:1 (0.3 M)	0.482	3.8 (78.8)	X	X	X	X	X	X
S. pasteurii	SP01-0.3 M	1:1 (0.3 M)	0.538	1.6 (29.7)	X	X		X	X	X
	SP02-0.02 M-D[c]	3:2 (0.02 M)	1.380	6.7 (48.3)					X	
	SP02-0.2 M-D	3:2 (0.2 M)						X	X	
	SP02-1 M-D	3:2 (1 M)						X	X	
	SP03-0.02 M-ND[c]	3:2 (0.02 M)	3.060	6.3 (20.5)					X	
	SP03-0.2 M-ND	3:2 (0.2 M)						X	X	
	SP03-1 M-ND	3:2 (1 M)						X	X	

[a] Names describe bacterial strain initials, test number as per equal OD_{600}, and total concentration of $CaCl_2$.
[b] Names describe whole ratios of urea to $CaCl_2$ followed by total concentration of $CaCl_2$.
[c] D and ND refer to diluted and non-diluted OD_{600}, respectively.

Table S4. MICP treatment formulations and characterisation details for the presenty study.